Aeroelastic Analysis of a Flexible Wing Wind Tunnel Model with Variable Camber Continuous Trailing Edge Flap Design

Nhan Nguyen *
NASA Ames Research Center, Moffett Field, CA 94035
Eric Ting †
Stinger Ghaffarian Technologies Inc., Moffett Field, CA 94035
Sonia Lebofsky ‡
Stinger Ghaffarian Technologies Inc., Moffett Field, CA 94035

This paper presents data analysis of a flexible wing wind tunnel model with a variable camber continuous trailing edge flap (VCCTEF) design for drag minimization tested at the University of Washington Aeronautical Laboratory (UWAL). The wind tunnel test was designed to explore the relative merit of the VCCTEF concept for improved cruise efficiency through the use of low-cost aeroelastic model test techniques. The flexible wing model is a 10%-scale model of a typical transport wing and is constructed of woven fabric composites and foam core. The wing structural stiffness in bending is tailored to be half of the stiffness of a Boeing 757-era transport wing while the torsional stiffness is about the same. This stiffness reduction results in a wing tip deflection of about 10% of the wing semi-span. The VCCTEF is a multi-segment flap design having three chordwise camber segments and five spanwise flap sections for a total of 15 individual flap elements. The three chordwise camber segments can be positioned appropriately to create a desired trailing edge camber. Elastomeric material is used to cover the gaps in between the spanwise flap sections, thereby creating a continuous trailing edge. Wind tunnel data analysis conducted previously shows that the VCCTEF can achieve a drag reduction of up to 6.31% and an improvement in the lift-to-drag ratio (L/D) of up to 4.85%. A method for estimating the bending and torsional stiffnesses of the flexible wing UWAL wind tunnel model from static load test data is presented. The resulting estimation indicates that the stiffness of the flexible wing is significantly stiffer in torsion than in bending by as much as 3 to 1. The lift prediction for the flexible wing is computed by a coupled aerodynamic-structural model. The coupled model is developed by coupling a conceptual aerodynamic tool Vorlax with a finite-element model of the flexible wing via an automated geometry deformation tool. Based on the comparison of the lift curve slope, the lift prediction for the rigid wing is in good agreement with the estimated lift coefficients derived from the wind tunnel test data. Due to the movement of the VCCTEF during the wind tunnel test, uncertainty in the lift prediction due to the indicated variations of the VCCTEF deflection is studied. The results show a significant spread in the lift prediction which contradicts the consistency in the aerodynamic measurements, thus suggesting that the indicated variations as measured by the VICON system may not be reliable. The lift prediction of the flexible wing agrees very well with the measured lift curve for the baseline configuration. The computed bending deflection and wash-out twist of the flexible wing also match reasonably well with the aeroelastic deflection measurements. The results demonstrate the validity of the aerodynamic-structural tool for use to analyze aerodynamic performance of flexible wings.

I. Introduction

The aircraft industry has been responding to the need for energy-efficient aircraft by redesigning airframes to be aerodynamically efficient, employing light-weight materials for aircraft structures and incorporating more energy-efficient aircraft engines. Reducing airframe operational empty weight (OEW) using advanced composite materials is one of the major considerations for improving energy efficiency. Modern light-weight materials can provide less structural rigidity while maintaining sufficient load-carrying capacity. As structural flexibility increases, aeroelastic interactions with aerodynamic forces and moments can alter aircraft aerodynamics significantly, thereby potentially degrading aerodynamic efficiency.

Under the Fundamental Aeronautics Program in NASA Aeronautics Research Mission Directorate, the Fixed Wing project is conducting multidisciplinary research to investigate advanced concepts and technologies for future aircraft systems. A NASA study entitled "Elastically Shaped Future Air Vehicle Concept" was conducted in 2010[1,2] to examine new concepts that can

*NASA Ames Research Center, Research Scientist, AIAA Associate Fellow, nhan.t.nguyen@nasa.gov
†Stinger Ghaffarian Technologies Inc., NASA Ames Research Center, Research Engineer, eric.b.ting@nasa.gov
‡Stinger Ghaffarian Technologies Inc., NASA Ames Research Center, Research Engineer, sonia.lebofsky@nasa.gov

enable active control of wing aeroelasticity to achieve drag reduction. This study showed that highly flexible wing aerodynamic surfaces can be elastically shaped in-flight by active control of wing twist and vertical deflection in order to optimize the local angles of attack of wing sections to improve aerodynamic efficiency through drag reduction during cruise and enhanced lift performance during take-off and landing.

The study shows that active aeroelastic wing shaping control can have a potential drag reduction benefit. Conventional flap and slat devices inherently generate drag as they increase lift. The study shows that conventional flap and slat systems are not aerodynamically efficient for use in active aeroelastic wing shaping control for drag reduction. A new flap concept, referred to as Variable Camber Continuous Trailing Edge Flap (VCCTEF) system, was conceived by NASA to address this need.[1] Initial study results indicate that, for some applications, the VCCTEF system may offer a potential pay-off in drag reduction that could provide significant fuel savings. In order to realize the potential benefit of drag reduction by active span-load and aeroelastic wing shaping control while meeting all other performance requirements, the approach for high lift devices needs to be considered as part of the wing shaping control strategy.

NASA and Boeing are currently conducting a joint study to develop the VCCTEF further under the research element Active Aeroelastic Shape Control (AASC) within the Fixed Wing project.[3,4] This study is built upon the development of the VCCTEF system for NASA Generic Transport Model (GTM) which is essentially based on the Boeing 757 airframe,[5] employing light-weight shaped memory alloy (SMA) technology for actuation and three separate chordwise segments shaped to provide a variable camber to the flap. This cambered flap has potential for drag reduction as compared to a conventional straight, plain flap. The flap is also made up of individual 2-foot spanwise sections which enable different flap setting at each flap spanwise position. This results in the ability to control the wing twist shape as a function of span, resulting in a change to the wing twist to establish the best lift-to-drag ratio (L/D) at any aircraft gross weight or mission segment. Wing twist on traditional commercial transport designs is dictated by the aeroelastic deflection of a fixed "jig twist" shape applied at manufacture. The design of this jig twist is set for one cruise configuration, usually for a 50% fuel loading or mid-point on the gross weight schedule. The VCCTEF offers different wing twist settings, hence different spanwise loadings, for each gross weight condition and also different settings for climb, cruise and descent, a major factor in obtaining best L/D conditions.

The second feature of VCCTEF is a continuous trailing edge flap. The individual 2-foot spanwise flap sections are connected with a flexible covering, so no breaks can occur in the flap planforms, thus reducing drag by eliminating these breaks in the flap continuity which otherwise would generate vorticity that results in a drag increase and also contributes to airframe noise. This continuous trailing edge flap design combined with the flap camber result in lower drag increase during flap deflections. In addition, it also offers a potential noise reduction benefit.

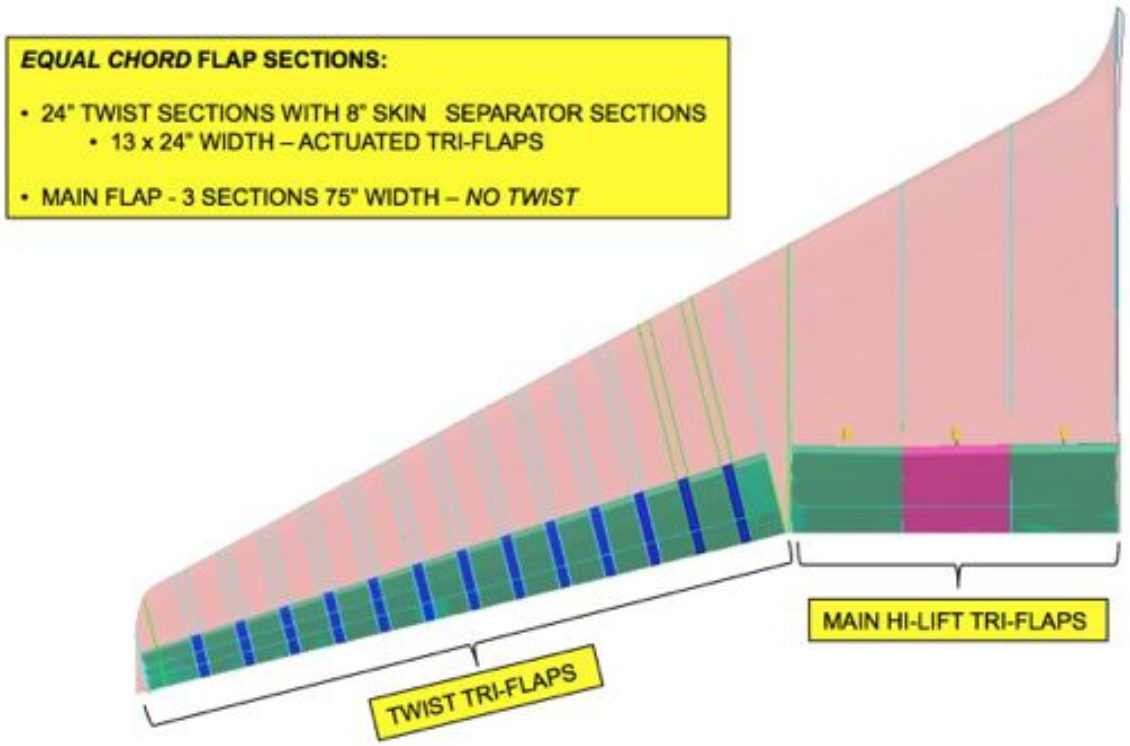

Fig. 1 - Wing Configured with the Variable Camber Continuous Trailing Edge Flap

The VCCTEF is divided into 14 sections attached to the outer wing and 3 sections attached to the inner wing, as shown in Fig. 1.[4] Each 24-inch section has three camber flap segments that can be individually commanded to form a variable camber

trailing edge, as shown in Fig. 2. These camber flaps are joined to the next section by a flexible and supported material (shown in blue) installed with the same shape as the camber and thus providing continuous flaps throughout the wing span with no drag producing gaps.

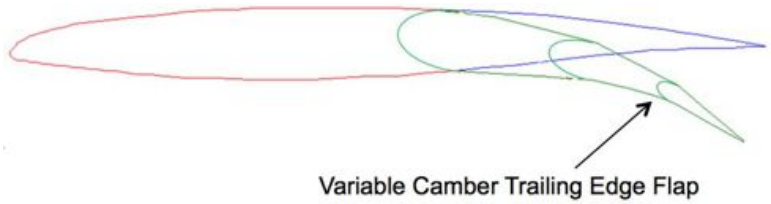

Fig. 2 - Variable Camber Flap

Using the camber positioning, a full-span, low-drag, high-lift configuration can be activated that has no drag producing gaps and a low flap noise signature. This is shown in Fig. 3. To further augment lift, a slotted flap configuration is formed by an air passage between the wing and the inner flap that serves to improve airflow over the flap and keep the flow attached. This air passage appears only when the flaps are extended in the high lift configuration.

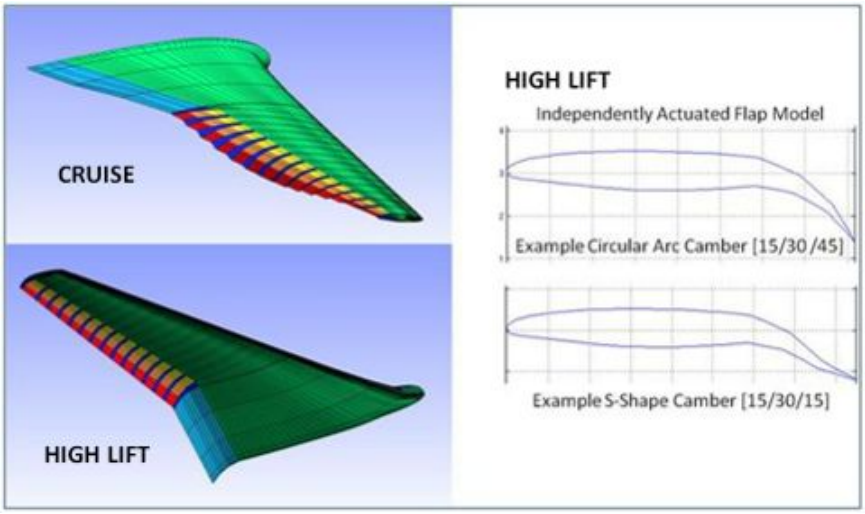

Fig. 3 - Cruise and High Lift VCCTEF Configurations

Figure 4 illustrates the GTM equipped with the VCCTEF for wing shaping control. By actively shaping the wing aerodynamic surface using the VCCTEF, optimal aerodynamic performance could potentially be realized at any point in the flight envelope. The VCCTEF relies on two mechanisms to improve aerodynamic performance: 1) wing twist optimization for flexible wing design, and 2) variable camber and continuous trailing edge for improved aerodynamics. This fixed-wing technology may be referred to as Performance Adaptive Aeroelastic Wing (PAAW) technology.

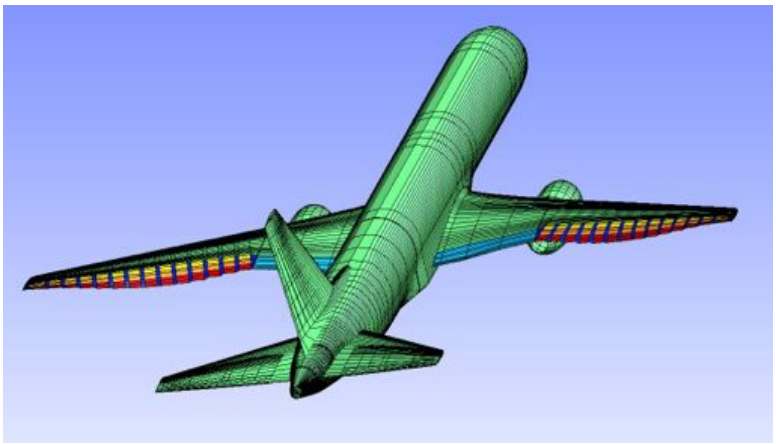

Fig. 4 - GTM with VCCTEF

II. Wind Tunnel Model of Flexible Wing with VCCTEF

For exploratory assessment of the aerodynamic potential of the VCCTEF concept, a 10%-scale aeroelastic model of a softened Boeing 757-based GTM wing was constructed for a wind tunnel experimental investigation in the University of Washington Aeronautical Laboratory (UWAL) in August of 2013.[6] The semi-span of the model is 5.6075 ft, as shown in Fig. 5. The model is constructed of woven fabric composites skin and extruded polystyrene foam core. The composite laminates and extruded polystyrene foam core are structurally tailored to attain half of the bending stiffness of the scaled baseline GTM wing stiffness while keeping torsional stiffness about the same. This tailored stiffness is to achieve a 10% wing tip deflection. The VCCTEF parts are fabricated by 3D printing. The flap segments are mechanically interlocking aerodynamic surfaces in the chordwise direction and mate with silicone elastomer material between spanwise flap sections, as shown in Fig. 6. The flap segments are hinged at three chordwise locations and are designed to be fully adjustable. The dimensions of the VCCTEF are shown in Fig. 7.

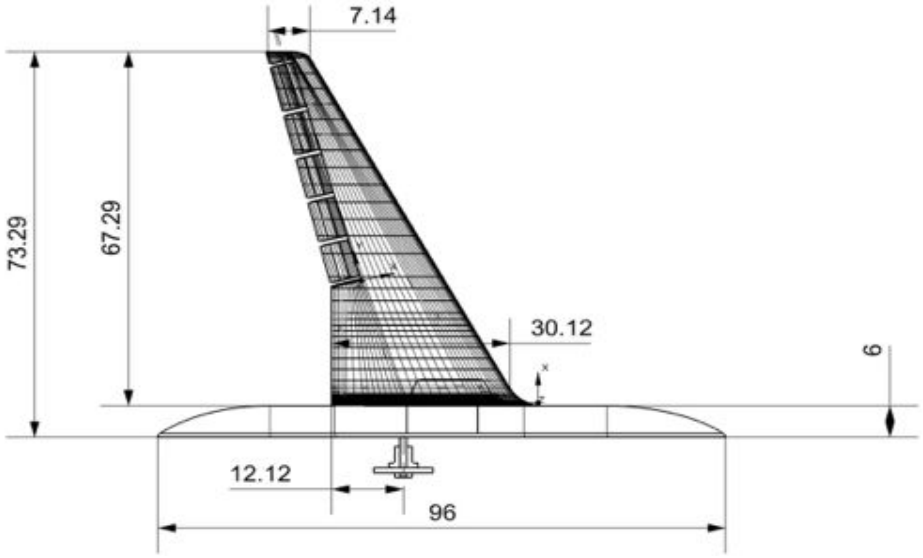

Fig. 5 - UWAL Wind Tunnel Model with VCCTEF (Courtesy of University of Washington Aeronautical Laboratory)

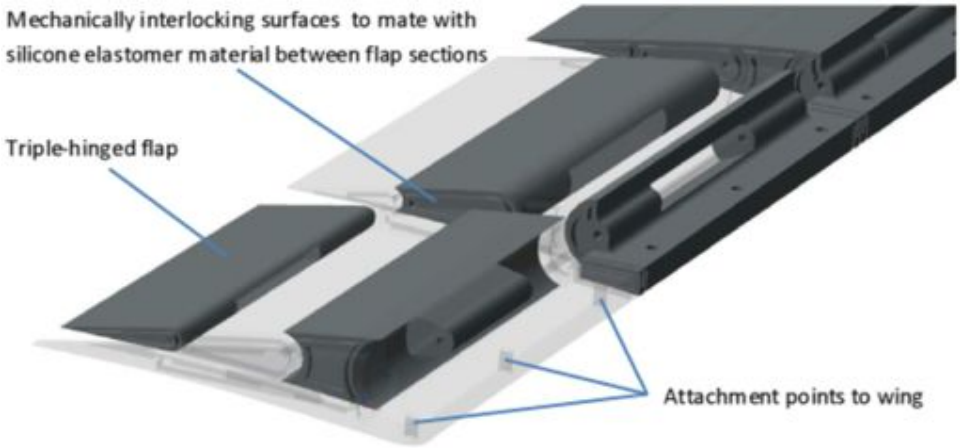

Fig. 6 - VCCTEF Construction (Courtesy of University of Washington Aeronautical Laboratory)

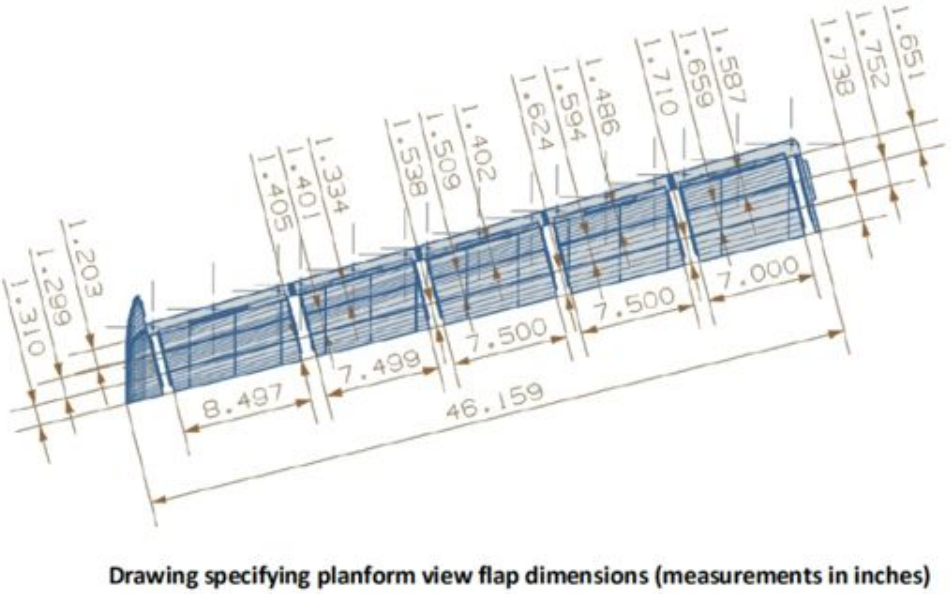

Fig. 7 - VCCTEF Dimension (Courtesy of University of Washington Aeronautical Laboratory)

Figure 8 shows an exploded view of the UWAL wind tunnel model of the flexible wing mated to a center body fairing attached to an external floor-mounted balance.

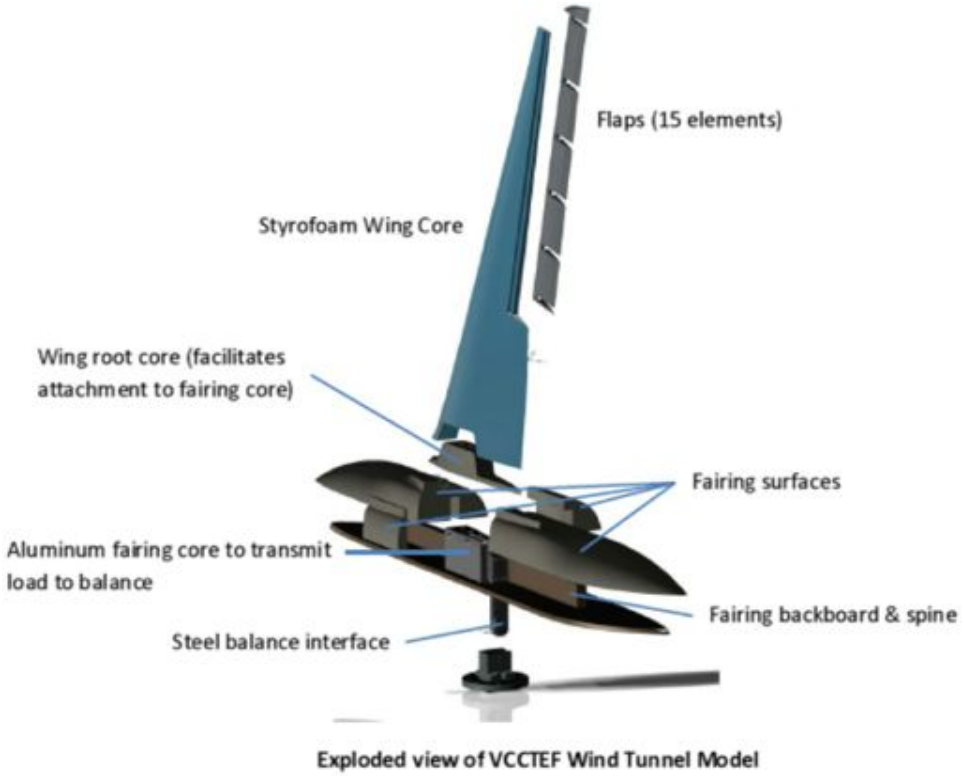

Fig. 8 - Exploded View of Wind Tunnel Model (Courtesy of University of Washington Aeronautical Laboratory)

The UWAL aeroelastic wind tunnel model was built with different stiffness than the scaled GTM wing and its jig shape was not optimized for best aerodynamic performance at test conditions. The same jig shape as that of the GTM wing was used. The wash-out twist is therefore non-optimal for the model when it operates at the design lift coefficient of 0.51. A CFD optimization was conducted prior to the test to identify an optimal jig twist. However, this optimized jig twist was not incorporated into the final model fabrication due to programmatic issues.

The relevant model scaling information is given in Table 1.

	Full-Scale	Semi-Span Model
M_∞	0.797	0.1162
C_L	0.51	0.51
h, ft	36,000	0
q_∞, psf	211.09	20.00
$S/2$, ft^2	975.5	9.638
$\bar{c}$, ft	16.6417	1.5963
$b/2$, ft	62.4167	6.1262

Table 1 - Model Parameters

The wind tunnel test is designed to be an exploratory, proof-of-concept study. The objective of the wind tunnel experiment is to explore the relative merit of the VCCTEF design as a drag reduction control device, and the ability to simulate the problem in a relatively low-cost test. Lift, drag, side force, pitching moment, yawing moment, and rolling moment were recorded from the external floor-mounted balance. In addition, aeroelastic deflections of the flexible wing model were also measured by a VICON motion tracking system. The VICON system measured the 3D displacement of the wind tunnel model at 54 points on the model.

To ensure that the wind tunnel model has correct aeroelastic properties, static load tests and frequency measurements were conducted. A detail 3D NASTRAN model was constructed by UWAL for comparison with the measurements.[6] The 3D NASTRAN results demonstrate an excellent agreement with the static load test data and measured frequencies. A stick NASTRAN model was also constructed by UWAL to match the deflection information from the 3D NASTRAN model. In addition, a NASTRAN Doublet Lattice flutter analysis was performed by UWAL to ensure that the wind tunnel is flutter-free in the wind tunnel.[6] Flutter speeds were determined to be well above the test section airspeed of 39.54 m/sec.

III. Wind Tunnel Test

The test was conducted at a nominal dynamic pressure of 20 psf. Off-condition data and additional runs at 10, 15, 25 and 30 psf were also collected for some cases. The nominal test section airspeed was Mach 0.1162. Figure 14 is a photograph of the flexible wing wind tunnel model in the UWAL test section.

Fig. 9 - Flexible Wing Wind Tunnel Model in UWAL Test Section (Courtesy of University of Washington Aeronautical Laboratory)

The wind tunnel model was tested with a total of 13 VCCTEF configurations ranging from zero to full deflection. These VCCTEF configurations are designated as:

- FLAP0 - baseline zero deflection
- FLAP1 - full deflection for all flap sections
- FLAP2 - varying from a maximum deflection at the inboard and outboard flaps to a minimum deflection at the mid-span flap
- FLAP3 - varying from a minimum deflection at the inboard and outboard flaps to a maximum deflection at the mid-span flap
- FLAP4 - varying monotonically from a maximum deflection at the inboard flap to zero deflection at the outboard flap
- FLAP5 - varying monotonically from zero deflection at the inboard flap to a maximum deflection at the outboard flap
- FLAP6 - similar to FLAP4 configuration but with a smaller deflection
- FLAP7 - varying monotonically from a maximum positive deflection at the inboard flap to a negative deflection at the outboard flap
- FLAP8 - rigid-body deflection with the two outer camber segments at zero relative deflection
- FLAP9 - deflection of the trailing edge camber segments
- FLAP10 - intermediate deflection
- FLAP11 - full negative deflection
- FLAP12 - FLAP6 configuration plus a gurney flap

Figure 10 illustrates some of these flap configurations.

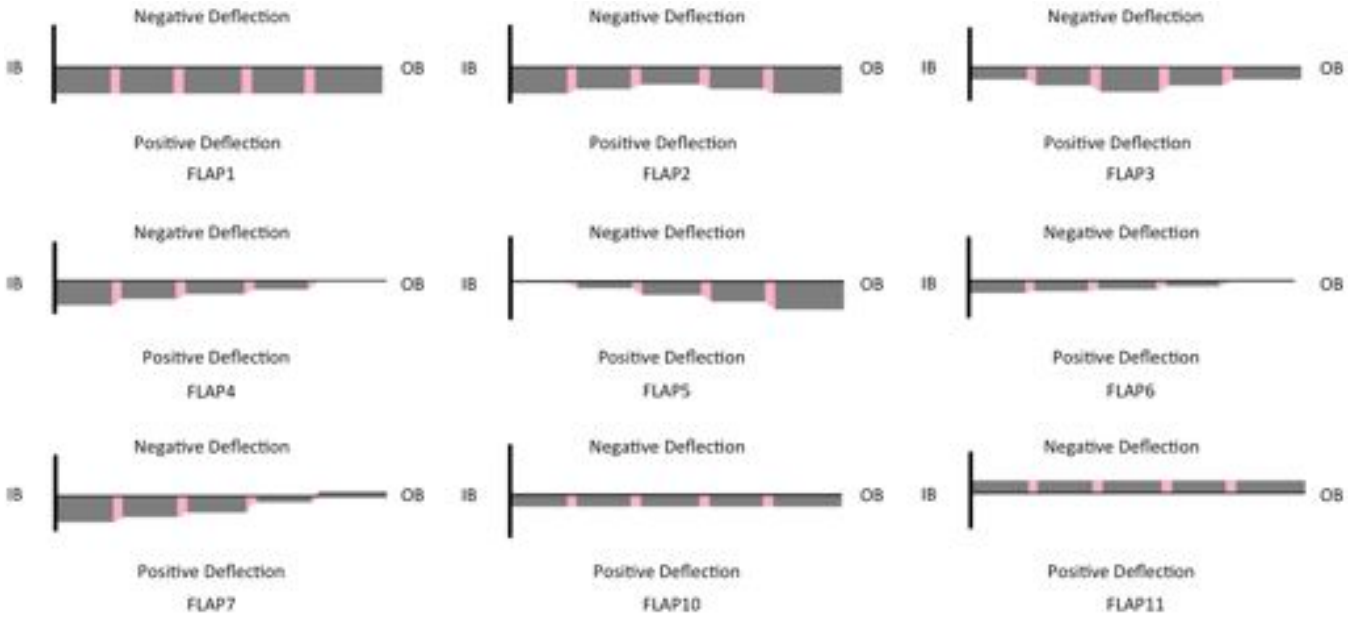

Fig. 10 - VCCTEF Flap Configurations (Courtesy of University of Washington Aeronautical Laboratory)

The test run matrix for the VCCTEF is shown in Table 2.

FLAP	0	1	2	3	4	5	6	7	8	9	10	11	12
$q_\infty = 0-20$ psf, $\alpha = 0^o$	18	25	32		42		55		73	79	86	93	
$q_\infty = 0-20$ psf, $\alpha = 1^o$	19	26	33	38	43	49	56	64	74	80	87 88	94	
$q_\infty = 0-20$ psf, $\alpha = 1.5^o$		27	34										
$q_\infty = 0-20$ psf, $\alpha = 2^o$	20	28	35	39	44	50	57	65	75	81	89	95	
$q_\infty = 0-20$ psf, $\alpha = 2.5^o$		29	36										
$q_\infty = 0-20$ psf, $\alpha = 3^o$		30		40	45	51	58	66	76	82	90	96	
$q_\infty = 0-20$ psf, $\alpha = 4^o$	22			41	46	52	59	67	77	83	91	97	
$q_\infty = 0-20$ psf, $\alpha = 4.5^o$					47	53							
$q_\infty = 0-20$ psf, $\alpha = 5^o$	23						60, 61	68	78	84	92	98	
$q_\infty = 0-20$ psf, $\alpha = 5.5^o$							62						
$q_\infty = 0-20$ psf, $\alpha = 6^o$												99	
$q_\infty = 0-20$ psf, $\alpha = 6.5^o$												100	
$q_\infty = 10$ psf, $\alpha = -2^o-10.5^o$	117							121					
$q_\infty = 15$ psf, $\alpha = -2^o-8.5^o$	118							122					
$q_\infty = 20$ psf, $\alpha = -2^o-7^o$	104 116	106 107					111	109 123				102	113
$q_\infty = 25$ psf, $\alpha = -2^o-5.5^o$	119							124					
$q_\infty = 30$ psf, $\alpha = -2^o-4.5^o$	120							125					

Table 2 - Test UW2087 Run Matrix

The VCCTEF segment positions for these configurations are shown in Table 3. The following convention is used. A flap section is a portion of the VCCTEF along the spanwise direction. There are 5 flap sections numbered from 1 at the inboard to 5 at the outboard. Each flap section is comprised of three camber segments labeled as A for the innermost camber segment, B for the middle camber segment, and C for the trailing edge camber segment. This is shown in Fig. 11. The position angle is denoted by $(a/b/c)$ where a, b, and c are flap positions in degrees relative to the forward flap segment. For segment A, the position angle is with respect to the fixed wing portion.

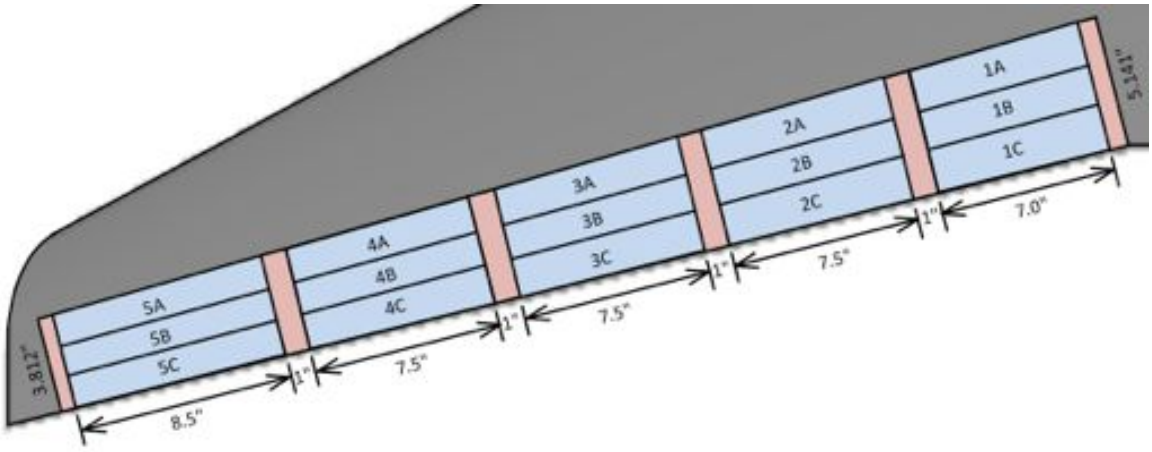

Fig. 11 - VCCTEF Flap Notation

FLAP	Run	Section 1	Section 2	Section 3	Section 4	Section 5
1	25	(5/4/9)	(6/7/9)	(9/7/10)	(7/8/10)	(6/9/9)
1*	106	(1/7/11)	(3/9/7)	(5/7/8)	(5/9/7)	(5/10/10)
1**	107	(1/7/11)	(3/9/7)	(5/7/8)	(5/9/7)	(5/10/10)
2	32	(3/2/10)	(4/5/4)	(5/3/4)	(4/6/5)	(5/10/10)
	36	(2/3/9)	(4/5/4)	(5/3/5)	(4/6/4)	(4/10/10)
3	38	(2/3/5)	(5/6/5)	(6/6/11)	(5/6/5)	(4/6/5)
	41	(2/3/5)	(4/6/5)	(4/6/11)	(4/6/5)	(3/6/5)
4	42	(2/5/9)	(3/6/3)	(4/1/6)	(2/5/2)	(0/0/0)
	47	(1/4/9)	(3/6/2)	(4/1/6)	(2/5/1)	(0/0/0)
5	49	(0/0/0)	(2/5/1)	(4/2/7)	(3/5/6)	(3/8/9)
	51	(0/0/0)	(2/5/1)	(4/2/7)	(3/5/6)	(3/8/9)
	53	(0/0/0)	(2/5/1)	(4/2/7)	(3/5/5)	(3/8/9)
6	55	(1/1/1)	(0/2/0)	(0/0/2)	(0/0/0.5)	(0/0/0)
	61	(1/1/1)	(0/2/0)	(0/0/2)	(0/0/0.5)	(0/0/0)
	62	(1/1/1)	(0/2/0)	(0/0/2)	(0/0/0.5)	(0/0/0)
	111	(1/1/1)	(0/1/1)	(0/0/2)	(0/0/0)	(0/0/0)
7	64	(3/3/4)	(2/3/2)	(0/0/3)	(0/0/0)	(0/0/−2)
7*	109	(3/4/3)	(2/5/1)	(2/0/2)	(0/−1/0)	(0/0/−2)
8	73	(4/0/0)	(4/0/0)	(5/0/0)	(5/0/0)	(4/0/0)
	78	(3/0/0)	(4/0/0)	(5/0/0)	(4/0/0)	(4/0/0)
9	79	(0/0/6)	(0/0/6)	(0/0/8)	(0/0/6)	(0/0/6)
	81	(0/0/6)	(0/0/6)	(0/0/8)	(0/0/6)	(0/0/6)
	84	(0/0/6)	(0/0/6)	(0/0/8)	(0/0/6)	(0/0/6)
10	86	(2/3/2)	(3/3/1)	(4/2/5)	(2/5/2)	(2/5/3)
	91	(2/3/2)	(3/3/1)	(4/2/5)	(2/5/2)	(2/5/3)
	92	(1/3/2)	(3/3/1)	(4/2/5)	(2/5/2)	(2/5/2)
11	93	(−1/0/−3)	(0/0/−6)	(−1/−4/0)	(−2/0/−5)	(−4/0/−4)
	100	(−1/0/−4)	(0/0/−5)	(−1/−3/0)	(−2/0/−5)	(−3/0/−4)

Table 3 - VCCTEF Deflections

IV. Aeroelastic Effects on Lift and Drag

The aeroelastic deflections of a flexible swept back wind tunnel model contribute significantly to the aerodynamic performance due to the wash-out effect resulting from wing bending and twist. Additionally, the VCCTEF deflections also contribute to angle of attack changes. The aeroelastic angle of attack of a wing section can be expressed as[7]

$$\alpha_c(y) = \alpha - \alpha_i(y) - \gamma(\bar{y})\cos\Lambda - \Theta(\bar{y})\cos\Lambda - \frac{dW(\bar{y})}{d\bar{y}}\sin\Lambda + \sum_{i=1}^{N}\frac{\partial\alpha_c}{\partial\delta_i}\delta_i(y_h)\cos\Lambda_h \tag{1}$$

where α is the geometric angle of attack of the wing section about the pitch axis y, α_i is the induced angle of attack due to the downwash about the pitch axis y, γ is the wing pre-twist angle about the elastic axis $\bar{y} = y/\cos\Lambda$ (positive nose down), Θ is the wing torsional twist about the elastic axis $\bar{y}$ (positive nose down), W is wing vertical bending along the elastic axis (positive upward), Λ is the sweep angle of the elastic axis, δ_i is the absolute deflection of the i-th flap segment of the VCCTEF about the hinge axis y_h which has a sweep angle of Λ_h, and $\partial\alpha_c/\partial\delta_i$ is the angle of attack sensitivity or camber control derivative due to the VCCTEF flap deflection.

The following convention is used. A quantity expressed with the independent variable y is one with respect to the streamwise direction, e.g., $c(y)$ is the sectional chord in the streamwise direction. A quantity expressed with the independent variable $\bar{y}$ is one with respect to the elastic axis; e.g., $\Theta(\bar{y})$ is the wing twist about the elastic axis. The quantity $\delta_i(y_h)$ is the flap deflection about the hinge axis.

In general, the aeroelastic deflections are functions of the angle of attack and the flap deflection. Therefore, they can be

expressed as

$$\Theta(\bar{y}) = \Theta_0(\bar{y}) + \frac{\partial \Theta(\bar{y})}{\partial \alpha}\alpha + \sum_{i=1}^{N} \frac{\partial \Theta(\bar{y})}{\partial \delta_i}\delta_i \tag{2}$$

$$W(\bar{y}) = W_0(\bar{y}) + \frac{\partial W(\bar{y})}{\partial \alpha}\alpha + \sum_{i=1}^{N} \frac{\partial W(\bar{y})}{\partial \delta_i}\delta_i \tag{3}$$

where Θ_0 and W_0 are the aeroelastic deflections at zero angle of attack, and the partial derivatives are the sensitivities of the aeroelastic deflections with respect to the angle of attack and the flap deflection.

Therefore, the expression for the aeroelastic angle of attack of a wing section can be written as

$$\begin{aligned}\alpha_c(y) = {} & \alpha\left[1 - \frac{\partial \Theta(\bar{y})}{\partial \alpha}\cos\Lambda - \frac{\partial}{\partial \alpha}\left(\frac{dW(\bar{y})}{d\bar{y}}\right)\sin\Lambda\right] - \alpha_i(y) - \gamma(\bar{y})\cos\Lambda - \Theta_0(\bar{y})\cos\Lambda - \frac{dW_0(\bar{y})}{d\bar{y}}\sin\Lambda \\ & + \sum_{i=1}^{N}\left[\frac{\partial \alpha_c}{\partial \delta_i}\cos\Lambda_h - \frac{\partial \Theta(\bar{y})}{\partial \delta_i}\cos\Lambda - \frac{\partial}{\partial \delta_i}\left(\frac{dW(\bar{y})}{d\bar{y}}\right)\sin\Lambda\right]\delta(y_h)\end{aligned} \tag{4}$$

It can be seen that the aeroelastic deflections can cause the desired sectional angle of attack to be non-optimal. The effect of the adaptive aeroelastic wing shaping control by the VCCTEF is captured in the last term. The term $\frac{\partial \alpha_c}{\partial \delta}$ is the rigid camber control to compensate for the non-optimal sectional angle of attack. The two terms $\frac{\partial \Theta}{\partial \delta}$ and $\frac{\partial}{\partial \delta}\left(\frac{dW}{d\bar{y}}\right)$ are the aeroelastic wing shaping control by leveraging wing flexibility to change the wash-out twist of a wing in order to achieve improved aerodynamic performance. Thus, the effect of adaptive aeroelastic wing shaping control is to optimize the span load at any operating point inside a given flight envelope.

The camber control derivative $\frac{\partial \alpha_c}{\partial \delta_i}$ can be directly estimated from thin airfoil potential flow theory by evaluating the following integral transform with the potential kernel function $f(\theta) = \cos\theta - 1$ as[8]

$$\frac{\partial \alpha}{\partial \delta_i} = -\frac{1}{\pi}\int_{\theta_i}^{\theta_{i+1}} f(\theta)\, d\theta = -\frac{1}{\pi}\int_{\theta_i}^{\theta_{i+1}} (\cos\theta - 1)\, d\theta \tag{5}$$

where

$$x' = \frac{c'}{2}(1 - \cos\theta) \tag{6}$$

$$c' - x_i' = \frac{c'}{2}(1 - \cos\theta_i) \tag{7}$$

and c' is the airfoil chord and x_i' is the flap hinge position of the i-th flap segment measured normal to the hinge axis from the trailing edge and is given by

$$x_i' = (n + 1 - i)\, c_f' \tag{8}$$

where c_f' is the flap chord of a camber segment measured normal to the hinge axis.

So the first hinge position is at $x_1' = Nc_f'$, the last hinge position is at $x_N' = c_f'$, and the trailing edge position is at $x_{N+1}' = 0$.

This integral is evaluated as

$$\frac{\partial \alpha_c}{\partial \delta_i} = \left.\frac{\cos^{-1}(-c^*) - \sqrt{1 - c^{*2}}}{\pi}\right|_{c_i^*}^{c_{i+1}^*} \tag{9}$$

where

$$c^* = 1 - 2\frac{x_i'}{c'} \tag{10}$$

The sectional lift coefficient is expressed as

$$c_L(y) = c_{L_0}(y) + c_{L_\alpha}(y)\left[\alpha(y) - \gamma(\bar{y})\cos\Lambda - \Theta(\bar{y})\cos\Lambda - \frac{dW(\bar{y})}{d\bar{y}}\sin\Lambda + \sum_{i=1}^{N}\frac{\partial \alpha_c}{\partial \delta_i}\delta_i(y_h)\cos\Lambda_h\right] \tag{11}$$

where c_{L_0} is the sectional lift coefficient at zero angle of attack and c_{L_α} is the sectional lift curve slope, both of which account for the induced angle of attack.

The sectional lift coefficient parameters c_{L_0} and c_{L_α} vary along the wing span and can be estimated from a three-dimensional aerodynamic analysis using a panel code or a CFD (Computational Fluid Dynamics) code.

Using aerodynamic strip theory, the total wing lift coefficient can be computed by integrating the local lift coefficient as follows:

$$C_L = \frac{1}{S}\int_{-b/2}^{b/2} c_L(y)\, c(y)\, dy \tag{12}$$

where c is the local chord length in the streamwise direction, and S is the wing reference area.

The lift coefficient can also be expressed in the standard form

$$C_L = C_{L_0}^* + C_{L_\alpha}^* \alpha + C_{L_\delta}^* \delta + \Delta C_{L_e} \tag{13}$$

where $C_{L_0}^*$ is the rigid lift coefficient at zero angle of attack, $C_{L_\alpha}^*$ is the rigid lift curve slope of finite-aspect ratio wing, $C_{L_\delta}^*$ is the vector of rigid lift coefficient sensitivities due to the VCCTEF deflection, $\delta = \begin{bmatrix} \delta_1 & \dots & \delta_N \end{bmatrix}^\top$ is the VCCTEF deflection vector, and ΔC_{L_e} is the incremental lift coefficients due to wing flexibility.

These quantities may be evaluated as

$$C_{L_0}^* = \frac{1}{S}\int_{-b/2}^{b/2} \left[c_{L_0}(y) - c_{L_\alpha}\gamma(y)\cos\Lambda\right] c(y)\, dy \tag{14}$$

$$C_{L_\alpha}^* = \frac{1}{S}\int_{-b/2}^{b/2} c_{L_\alpha}(y)\, c(y)\, dy \tag{15}$$

$$C_{L_\delta}^* = \frac{1}{S}\int_{-b/2}^{b/2} c_{L_\alpha}(y)\, \frac{\partial \alpha_c}{\partial \delta}\cos\Lambda_h c(y)\, dy \tag{16}$$

$$\Delta C_{L_e} = \frac{1}{S}\int_{-b/2}^{b/2} c_{L_\alpha}(y) \left[-\Theta(\bar{y})\cos\Lambda - \frac{dW(\bar{y})}{d\bar{y}}\sin\Lambda\right] c(y)\, dy \tag{17}$$

where $\frac{\partial \alpha_c}{\partial \delta} = \begin{bmatrix} \frac{\partial \alpha_c}{\partial \delta_1} & \dots & \frac{\partial \alpha_c}{\partial \delta_N} \end{bmatrix}$.

The aeroelastic deflections of a wing can be modeled by the following equations:

$$\frac{\partial}{\partial \bar{y}}\left\{\left[GJ + EB_1\left(\gamma'\right)^2\right]\frac{\partial \Theta}{\partial \bar{y}} - EB_2\gamma'\frac{\partial^2 W}{\partial \bar{y}^2}\right\} = \left[\left(c_{m_{ac}} + c_{m_\delta}\delta\right)c + \frac{e}{\cos\Lambda}c_L\right] q_\infty \cos^2\Lambda c \tag{18}$$

$$\frac{\partial^2}{\partial \bar{y}^2}\left(EI\frac{\partial^2 W}{\partial \bar{y}^2} - EB_2\gamma'\frac{\partial \Theta}{\partial \bar{y}}\right) = c_L q_\infty \cos\Lambda c \tag{19}$$

where e is the aerodynamic center offset measured perpendicular to the elastic axis, $c_{m_{ac}}$ is the sectional pitching moment coefficient about the aerodynamic center defined in the streamwise direction, c_{m_δ} is the vector of pitching moment coefficient sensitivities about the aerodynamic center defined in the streamwise direction for the VCCTEF, and B_1 and B_2 are the bending-torsion coupling constants which are generally small for slightly twisted wings and therefore are usually neglected.

Using thin airfoil potential flow theory, the pitching moment coefficient sensitivity about the aerodynamic center, which is taken to be at the quarter-chord location, of the i-th flap segment can be estimated using a kernel function $g(\theta) = \cos 2\theta - \cos\theta$ as

$$c_{m_{\delta_i}} = -\frac{c_{L_\alpha}}{4\pi}\int_{\theta_i}^{\theta_{i+1}} (\cos 2\theta - \cos\theta)\, d\theta \tag{20}$$

where c_{L_α} is the sectional lift curve slope from Eq. (11).

This results in a theoretical expression as

$$c_{m_{\delta_i}} = \left.\frac{c_{L_\alpha}(1+c^*)\sqrt{1-c^{*2}}}{4\pi}\right|_{c_i^*}^{c_{i+1}^*} \tag{21}$$

The Kutta-Joukowski theorem states that, for a two-dimensional airfoil, the lift force per unit length is $L = \rho_\infty V_\infty \Gamma$, where Γ is the circulation.[8] Then, from Eq. (11), the lift circulation is defined as

$$\begin{aligned}\Gamma(y) &= \frac{1}{2}V_\infty c_L(y)\, c(y) \\ &= \frac{1}{2}V_\infty\left\{c_{L_0}(y) + c_{L_\alpha}(y)\left[\alpha - \gamma(\bar{y})\cos\Lambda - \Theta(\bar{y})\cos\Lambda - \frac{dW(\bar{y})}{d\bar{y}}\sin\Lambda + \sum_{i=1}^{N}\frac{\partial \alpha_c}{\partial \delta_i}\delta_i(y_h)\cos\Lambda_h\right]\right\} c(y)\end{aligned} \tag{22}$$

The lift circulation shows that the aeroelastic deflections can influence the spanwise lift distribution, hence induced drag. As a wing becomes more flexible, aeroelastic deflections at off-design cruise conditions can cause induced drag penalty. By controlling the aeroelastic deflections using the VCCTEF, the spanwise lift distribution can be tailored for off-design aerodynamic performance. It should be noted that the VCCTEF can provide the same potential benefit for a stiff and, in the limit, even rigid wing design since the VCCTEF can directly alter the spanwise lift distribution via camber control. To achieve optimal off-design aerodynamic performance, a multi-disciplinary optimization can be conducted to determine the optimal VCCTEF deflections at functions of flight conditions inside a flight envelope. As a matter of fact, the very terminology of "design" and "off-design" flight conditions may need to be revised, since with the VCCTEF it might be possible to approach optimal lift-to-drag ratios at many flight conditions.

For a flexible swept back wing, the bending slope $\frac{dW}{d\bar{y}}$ which is normally positive causes a local wing wash-out twist which decreases the sectional angle of attack. As a result, the lift coefficient generally decreases at a given aircraft angle of attack when compared to the lift coefficient for a rigid wing. Therefore, to achieve the same lift coefficient, an increase in the angle of attack is required to compensate for the aeroelastic effect.

To model the aeroelastic effects, various modeling approaches are used. A standard approach is to use a finite-element model coupled with an aerodynamic solver such as a panel code or a CFD code. To use the finite-element method, the structural properties of a wing need to be established accurately. This information is then used to predict the aeroelastic deflection. Even though such a method is considered to be standard, the modeling accuracy can still be subject to high uncertainty. Stiffness uncertainty as well as aerodynamic prediction uncertainty can result in inaccurate results.

One approach to reducing modeling uncertainty in the data analysis using strictly experimental data is the Galerkin's method. The Galerkin's method uses a series approximation of mode shapes using the analytical mode shapes of a simpler structure with the same boundary conditions. For a cantilever wing, the mode shapes can be approximated by a series of analytical mode shapes of a uniform cantilever beam.[9] Since no structural information about the stiffness is required and the aeroelastic deflection measurements are available, the Galerkin's method is well suited for use in the data analysis. The resulting formulation can add insight into the various physical effects involved in the wind tunnel test. A standard finite-element aerodynamic panel solution is presented in the paper by Precup, Mor, and Livne.[6] In addition, a preliminary static aeroelastic analysis was also conducted by Rodriguez, Aftosmis, Nemec, and Smith using Cart3D inviscid CFD code coupled with a structural beam model.[10] This paper presents an aeroelastic study of the flexible wing UWAL wind tunnel model using a finite-element modeling method coupled to a vortex-lattice aerodynamic solver developed by Nguyen, Ting, et al.[11,12]

The general solution of the coupled bending-torsion aeroelasticity can be expressed as

$$\Theta(\bar{y}) = \Psi(\bar{y})\,\theta \tag{23}$$

$$W(\bar{y}) = \Phi(\bar{y})\,w \tag{24}$$

where $\Psi(\bar{y}) = \begin{bmatrix} \psi_1(\bar{y}) & \dots & \psi_n(\bar{y}) \end{bmatrix}$ and $\Phi(\bar{y}) = \begin{bmatrix} \phi_1(\bar{y}) & \dots & \phi_n(\bar{y}) \end{bmatrix}$ are mode shape functions, and $\theta = \begin{bmatrix} \theta_1 & \dots & \theta_n \end{bmatrix}^\top$ and $w = \begin{bmatrix} w_1 & \dots & w_n \end{bmatrix}^\top$ are generalized displacements which can be solved from

$$\begin{aligned} \begin{bmatrix} \theta \\ w \end{bmatrix} &= \begin{bmatrix} K_{s_{\theta\theta}} + K_{a_{\theta\theta}} & K_{a_{\theta w}} \\ K_{a_{w\theta}} & K_{s_{ww}} + K_{a_{ww}} \end{bmatrix}^{-1} \left\{ \begin{bmatrix} F_{\theta_0} \\ F_{w_0} \end{bmatrix} + \begin{bmatrix} F_{\theta\alpha} \\ F_{w\alpha} \end{bmatrix} \alpha + \begin{bmatrix} F_{\theta\delta} \\ F_{w_0} \end{bmatrix} \delta \right\} \\ &= \begin{bmatrix} \theta_0 \\ w_0 \end{bmatrix} + \frac{\partial}{\partial \alpha} \begin{bmatrix} \theta \\ w \end{bmatrix} \alpha + q_\infty \frac{\partial}{\partial \delta} \begin{bmatrix} \theta \\ w \end{bmatrix} \delta \end{aligned} \tag{25}$$

Note that the stiffness matrices $K_{a_{\theta\theta}}$, $K_{a_{\theta w}}$, $K_{a_{w\theta}}$, and $K_{a_{ww}}$ are dependent on q_∞. For low dynamic pressure well below the divergence dynamic pressure, the stiffness matrix inversion can be approximated as

$$\left(K_s + q_\infty \frac{K_a}{q_\infty}\right)^{-1} = K_s^{-1} - q_\infty K_s^{-1} \frac{K_a}{q_\infty} K_s^{-1} \left(I + q_\infty \frac{K_a}{q_\infty} K_s^{-1}\right)^{-1} \tag{26}$$

$$\approx K_s^{-1} - q_\infty K_s^{-1} \frac{K_a}{q_\infty} K_s^{-1} + q_\infty^2 K_s^{-1} \frac{K_a}{q_\infty} K_s^{-1} \frac{K_a}{q_\infty} K_s^{-1} \tag{27}$$

where $\frac{K_a}{q_\infty}$ is the aerodynamic generalized influence coefficients matrix which is independent of q_∞.

Thus, the aeroelastic deflections are obtained as functions of the angle of attack and the flap deflections as

$$\Theta(\bar{y}) = \Psi(\bar{y}) \left[\left(A_{0_\theta} + A_{\alpha_\theta}\alpha + A_{\delta_\theta}\delta\right) q_\infty + \left(B_{0_\theta} + B_{\alpha_\theta}\alpha + B_{\delta_\theta}\delta\right) q_\infty^2 + \left(C_{0_\theta} + C_{\alpha_\theta}\alpha + C_{\delta_\theta}\delta\right) q_\infty^3 \right] \tag{28}$$

$$W(\bar{y}) = \Phi(\bar{y}) \left[\left(A_{0_w} + A_{\alpha_w}\alpha + A_{\delta_w}\delta\right) q_\infty + \left(B_{0_w} + B_{\alpha_w}\alpha + B_{\delta_w}\delta\right) q_\infty^2 + \left(C_{0_w} + C_{\alpha_w}\alpha + C_{\delta_w}\delta\right) q_\infty^3 \right] \tag{29}$$

Thus, the lift coefficient of a flexible wing is expressed as

$$C_L = C_L^* + (a_0 + a_\alpha \alpha + a_\delta \delta) q_\infty + (b_0 + b_\alpha \alpha + b_\delta \delta) q_\infty^2 + (c_0 + c_\alpha \alpha + c_\delta \delta) q_\infty^3 \tag{30}$$

where C_L^* is the rigid-wing lift coefficient and the remaining terms are due to the effect of aeroelasticity and

$$a_{(0,\alpha,\delta)} = \frac{1}{S} \int_{-b/2}^{b/2} c_{L_\alpha}(y) \left[-\Psi(\bar{y}) A_{(0,\alpha,\delta)_\theta} \cos\Lambda - \frac{d\Phi(\bar{y})}{d\bar{y}} A_{(0,\alpha,\delta)_w} \sin\Lambda \right] c(y)\, dy \tag{31}$$

$$b_{(0,\alpha,\delta)} = \frac{1}{S} \int_{-b/2}^{b/2} c_{L_\alpha}(y) \left[-\Psi(\bar{y}) B_{(0,\alpha,\delta)_\theta} \cos\Lambda - \frac{d\Phi(\bar{y})}{d\bar{y}} B_{(0,\alpha,\delta)_w} \sin\Lambda \right] c(y)\, dy \tag{32}$$

$$c_{(0,\alpha,\delta)} = \frac{1}{S} \int_{-b/2}^{b/2} c_{L_\alpha}(y) \left[-\Psi(\bar{y}) C_{(0,\alpha,\delta)_\theta} \cos\Lambda - \frac{d\Phi(\bar{y})}{d\bar{y}} C_{(0,\alpha,\delta)_w} \sin\Lambda \right] c(y)\, dy \tag{33}$$

Note that these integral are evaluated in the wing pitch axis $y \in \left[0, \frac{b}{2}\right]$.

Equation (30) can be used to estimate the rigid wing lift coefficients. Note that if a swept back wing experiences a nose-down twist ($\Psi(\bar{y}) > 0$) and upward bending $\left(\frac{d\Phi(\bar{y})}{d\bar{y}} > 0\right)$, then the terms $a_{(0,\alpha,\delta)}$ are negative since they are due to the positive terms $A_{(0,\alpha,\delta)_\theta}$ and $A_{(0,\alpha,\delta)_w}$ which come from K_s^{-1} which is always positive.

Note that when $q_\infty = 0$, $C_L = C_L^*$. This suggests that one can estimate the rigid-wing lift coefficient by analyzing the lift coefficient variation with the dynamic pressure.

If the dynamic pressure is held constant and if aeroelastic deflection measurements are available, then this information can also be used to estimate the rigid-wing lift coefficient. In this case, the effective lift coefficient parameters are expressed as

$$C_{L_0} = C_{L_0}^* - \frac{1}{S} \int_{-b/2}^{b/2} c_{L_\alpha}(y) \left[\Theta_0(\bar{y}) \cos\Lambda + \frac{dW_0(\bar{y})}{d\bar{y}} \sin\Lambda \right] c(y)\, dy \tag{34}$$

$$C_{L_\alpha} = C_{L_\alpha}^* - \frac{1}{S} \int_{-b/2}^{b/2} c_{L_\alpha}(y) \left[\frac{\partial \Theta(\bar{y})}{\partial \alpha} \cos\Lambda + \frac{\partial}{\partial \alpha} \left(\frac{dW(\bar{y})}{d\bar{y}} \right) \sin\Lambda \right] c(y)\, dy \tag{35}$$

$$C_{L_\delta} = C_{L_\delta}^* - \frac{1}{S} \int_{-b/2}^{b/2} c_{L_\alpha}(y) \left[\frac{\partial \Theta(\bar{y})}{\partial \delta} \cos\Lambda + \frac{\partial}{\partial \delta} \left(\frac{dW(\bar{y})}{d\bar{y}} \right) \sin\Lambda \right] c(y)\, dy \tag{36}$$

Since Θ and $\frac{dW}{d\bar{y}}$ are generally positive for a wing with positive lift, the effect of aeroelasticity on a swept back wing is to reduce lift and lift coefficient sensitivity due to a flap deflection.

V. Summary of Wind Tunnel Experimental Data

There was a total of 125 useful test runs. Test data consist of force, moment, and aeroelastic deflection measurements, and were collected during α-sweep and q_∞-sweep runs. For clarity, α is the angle of attack of the flexible wing wind tunnel model, which is defined as the angle between incoming air and the root attachment of the wing. The force and moment measurements were provided by the external balance. The aeroelastic deflection measurements were provided by the VICON motion tracking system. The nominal dynamic pressure is 20 psf. The full report of the wind tunnel test data analysis is published by Nguyen et al.[13]

For summary, only test data for FLAP0 configuration is shown. The lift curve and drag polar for the baseline FLAP0 configuration are plotted in Figs. 12 and 13. The data come from 20 different runs. As can be seen, the data show high degree of repeatability and correlation.

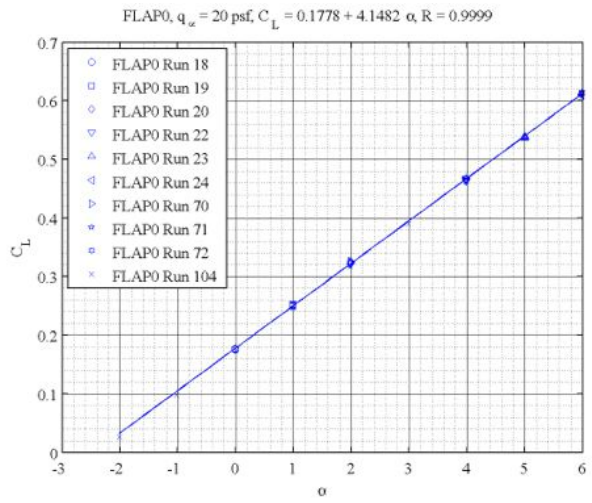

Fig. 12 - FLAP0 C_L vs. α

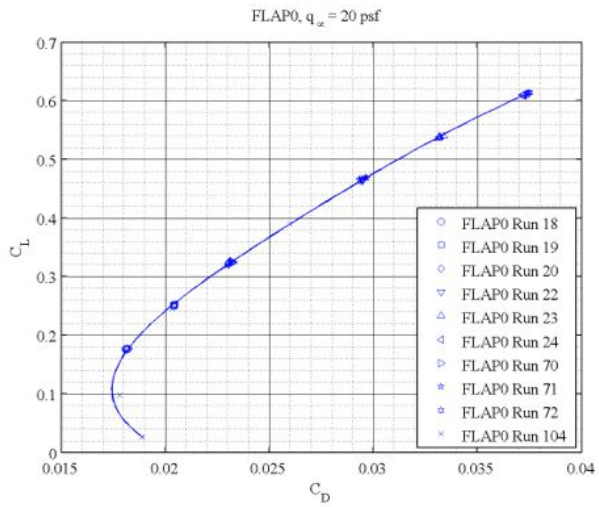

Fig. 13 - FLAP0 C_L vs. C_D

Figures 14 and 15 are the plots of L/D for FLAP0, FLAP1, FLAP7, and FLAP11 configurations. The baseline FLAP0 configuration has a L/D value of about 16.1 at $C_L = 0.51$. FLAP1 configuration has the highest L/D at the same C_L as compared to all the other VCCTEF configurations. Its L/D is about 17.2 which is about a 6.8% improvement. FLAP11 configuration is not aerodynamically efficient since it is configured as a lift-reduction device with negative VCCTEF deflections.

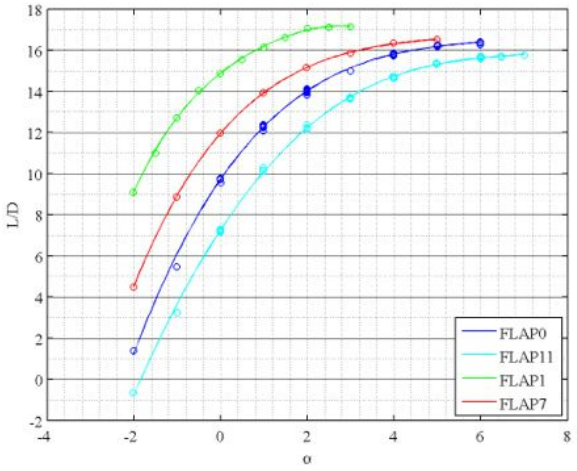

Fig. 14 - L/D vs. α

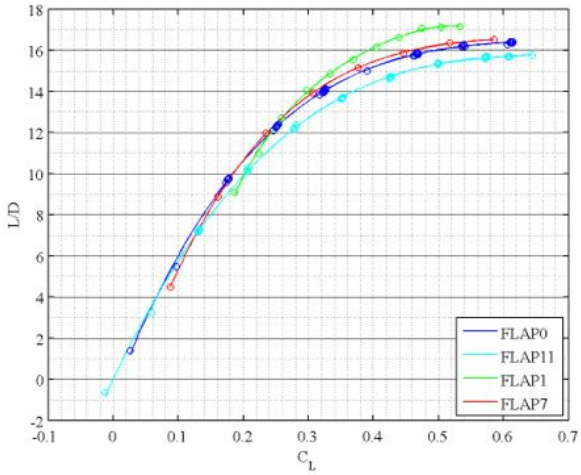

Fig. 15 - L/D vs. C_L

Table 4 presents the summary of the drag comparison for all the VCCTEF configurations. As can be seen, FLAP1 configuration is the most aerodynamically efficient, achieving a maximum of 6.31% drag reduction at the design cruise C_L. All VCCTEF configurations except FLAP11 and FLAP12 achieve varying degree of drag reduction. In terms of the absolute values of L/D, the maximum increase in L/D is 4.85% due to FLAP1 configuration.

FLAP	C_D @ $C_L = 0.51$ (Counts)	C_D Reduction (Counts)	% Drag Reduction	L/D Max	% L/D Increase
0	317	0	0	16.4182	0
1	303	14	4.42	17.2151	4.85
1*	298	19	5.99	17.1337	4.36
1**	297	20	6.31	17.1553	4.49
2	301	16	5.05	17.0012	3.55
3	300	17	5.36	17.1285	4.33
4	308	9	2.84	16.8104	2.39
5	304	13	4.10	16.9709	3.37
6	313	4	1.26	16.6054	1.14
7	313	4	1.26	16.6340	1.31
7*	312	5	1.58	16.5125	0.57
8	311	6	1.89	16.7022	1.73
9	305	12	3.79	16.9840	3.45
10	307	10	3.15	16.9420	3.19
11	331	-14	-4.42	15.7418	-4.12
12	326	-9	-2.84	16.1385	-1.70

Table 4 - Summary of Drag Reduction an L/D Improvements of VCCTEF (1 Drag Count = 0.0001)

Figure 16 shows the lift coefficient sensitivity to the dynamic pressure. As thy dynamic pressure increases, the lift coefficient decreases. By extrapolation of the data to $q_\infty = 0$, one can estimate the rigid wing lift coefficient. Both linear and cubic polynomial extrapolation were used to correct the flexible wing lift curves to obtain the rigid wing lift curves, as shown in Fig. 17. The cubic polynomial method is supposed to yield more accurate estimates according to Eq. (30).

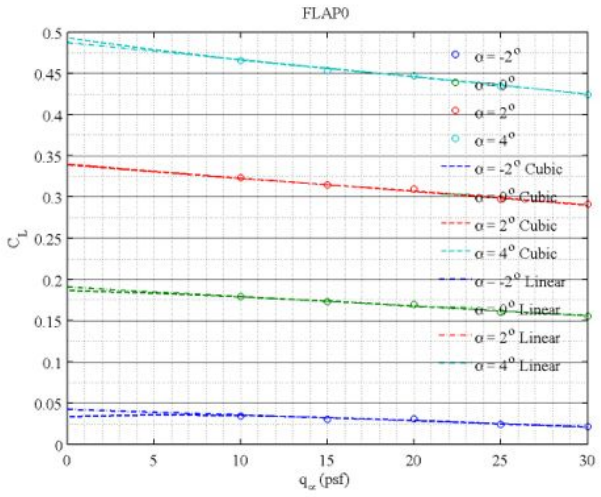

Fig. 16 - FLAP0 Cubic and Linear Variations of C_L with q_∞

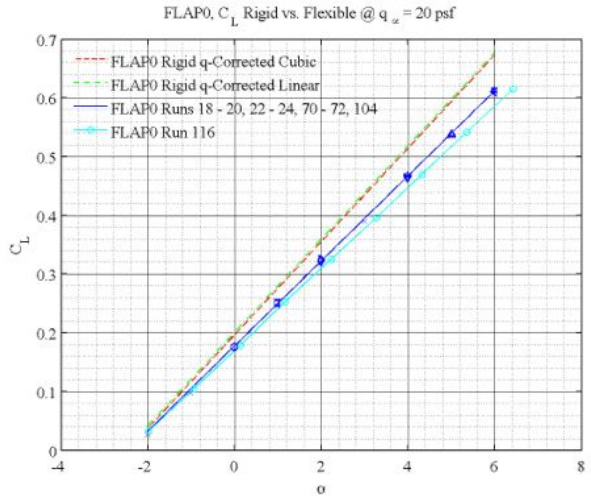

Fig. 17 - FLAP0 Runs 18 - 20, 22 - 24, 70 - 72, 104 C_L of Flexible and Rigid Wing

The effect of aeroelasticity on the lift coefficient is also analyzed. The measured wing bending deflection, bending slope, and torsional deflection about the elastic axis of FLAP0 configuration are shown in Fig. 18, 19, and 20.

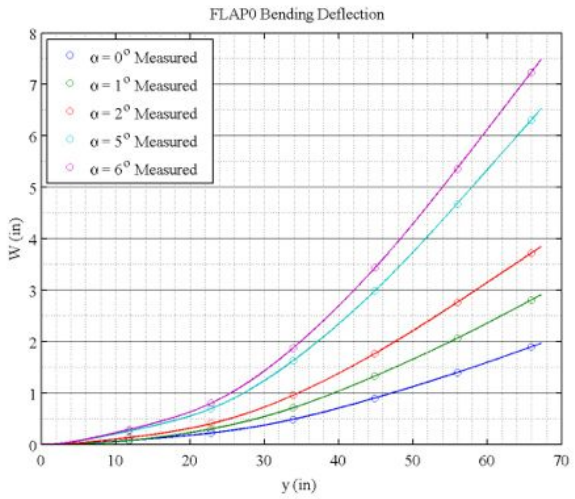

Fig. 18 - FLAP0 Bending Deflection

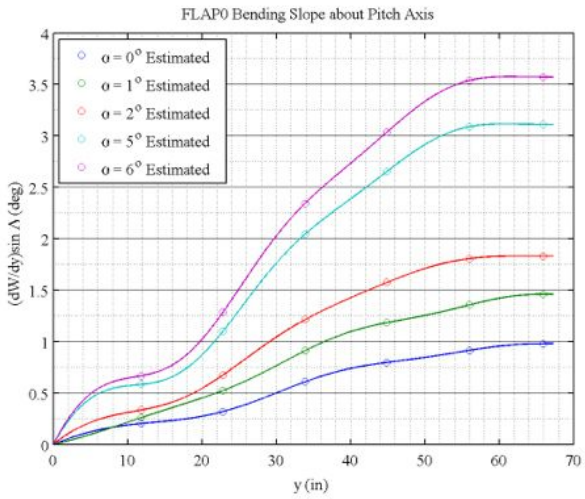

Fig. 19 - FLAP0 Bending Slope about Pitch Axis

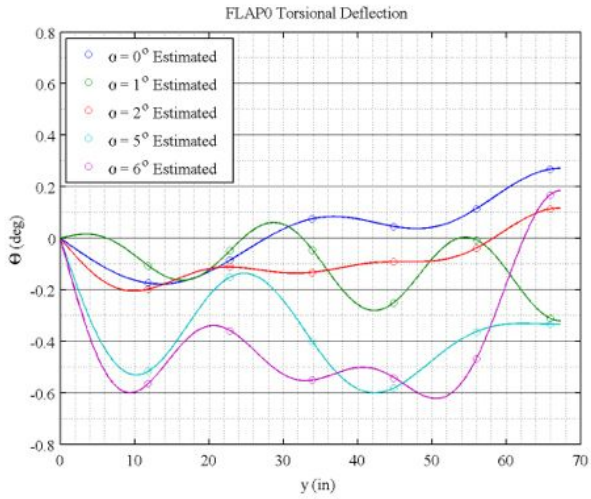

Fig. 20 - FLAP0 Torsional Deflection

The rigid wing lift coefficient can be estimated from the static bending and torsional deflections of the wing. The wing aeroelastic deflection results in an effective change in the angle of attack, which is computed as[13]

$$\Delta\alpha = -\frac{1}{C^*_{L\alpha} S}\int_{-b/2}^{b/2} c^*_{L_\alpha}(y)\left[\Theta(\bar{y})\cos\Lambda + \frac{dW(\bar{y})}{d\bar{y}} w \sin\Lambda\right] c(y)\, dy \tag{37}$$

where $c^*_{L_\alpha}(y)$ is the sectional lift curve slope for the rigid wing.

This effective change in the angle of attack is a function of the angle of attack as

$$\Delta\alpha = \Delta\alpha_0 + \frac{\partial\Delta\alpha}{\partial\alpha}\alpha \tag{38}$$

By making an assumption that $c^*_{L_\alpha}(y) = C^*_{L_\alpha}$, the rigid wing lift coefficient can be computed from the flexible wing lift coefficient as[13]

$$C^*_L = C_L - \frac{C_{L_\alpha}\Delta\alpha}{1 + \frac{\partial\Delta\alpha}{\partial\alpha}} \tag{39}$$

Figure 21 shows the rigid wing lift coefficients estimated by the aeroelastic deflection correction method and the two q_∞-correction methods as compared to the flexible wing lift coefficient.[13] The aeroelastic deflection correction method yields the highest estimated rigid-wing lift coefficient. Since there are some differences in the three estimated rigid wing lift coefficients, an average rigid wing lift coefficient is computed and is shown in Fig. 21.

Both the aeroelastic deflection correction method and the q_∞-correction method exhibit some degree of uncertainty. For the aeroelastic deflection correction method, the assumption of the sectional lift curve slope being the same as the wing lift curve slope is made. This assumption needs to be verified by aerodynamic analysis using CFD. Also, the aeroelastic deflection measurements have uncertainty associated with the accuracy of the VICON system. For the q_∞-correction method, data extrapolation can result in less robust estimation if there are not sufficient data to establish the confidence. Figure 16 shows a good correlation in the lift coefficient as a function of the dynamic pressure that is consistent with the aeroelastic analysis. Thus, this establishes a degree of confidence in the q_∞-correction method. Also, depending on the type of regressors such as the cubic and linear functions, the results can differ. Nonetheless, in the estimation, both the linear and cubic functions yield similar results.

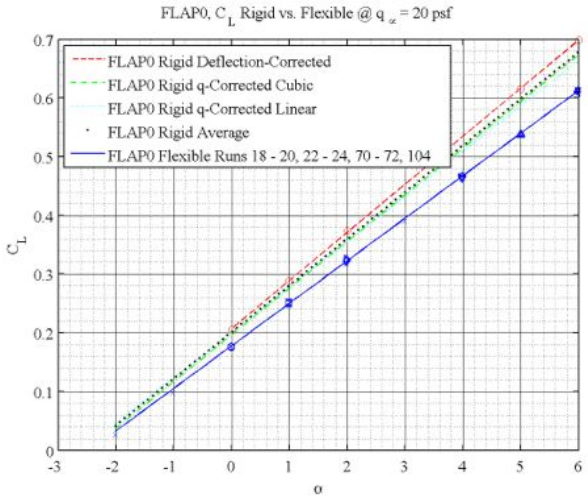

Fig. 21 - FLAP0 Runs 18 - 20, 22 - 24, 70 - 72, 104 C_L of Flexible and Rigid Wing

VI. Aeroelastic Deflection Measurements and Wing Stiffness Estimation

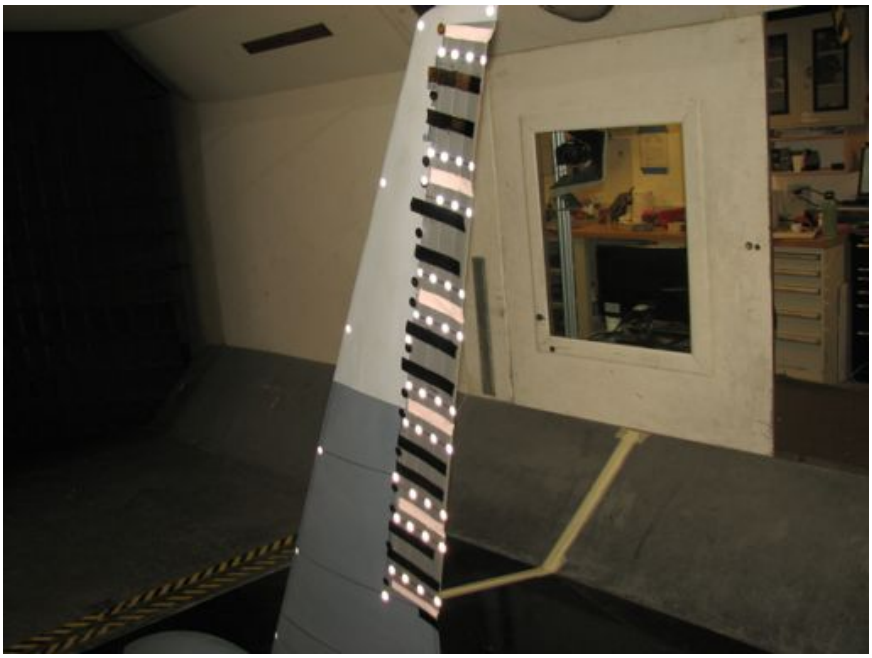

Fig. 22 - Wind Tunnel Model with VICON Dots in UWAL Test Section (Courtesy of University of Washington)

Aeroelastic deflection measurements were taken with the VICON motion tracking system. The VICON system uses 54 optical targets, called dots, to create a three-dimensional displacement of the wind tunnel model as it is loaded. Figure 22 is a photograph of the wind tunnel model with the VICON dots. The displacement measurements at these dots are reduced to the spanwise out-of-plane deflections and twists at six spanwise locations, referred to as Chord 1, Chord 2, Chord 3, Chord

4, Chord 5, and Chord 6, as shown in Fig. 23. The deflection measurement locations are referenced to the origin of the wind tunnel model which starts at the intersection of the wing trailing edge and the center body.

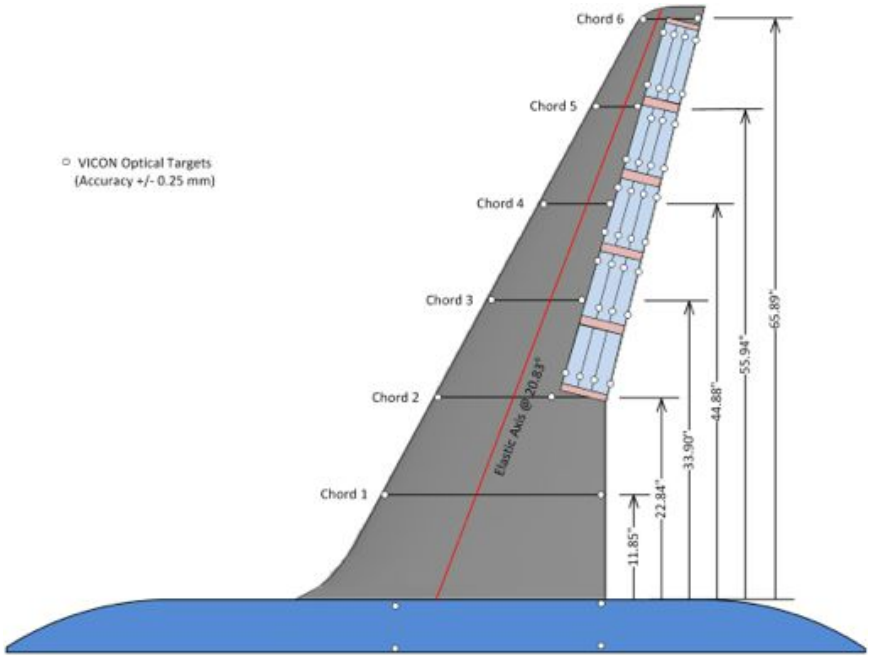

Fig. 23 - VICON Target and Spanwise Deflection Measurement Locations

A series of static load and modal analysis tests were performed prior to the wind tunnel test runs. The static load tests were conducted by applied concentrated loads at two wing span stations $y = 60.75$ inches and $y = 25.75$ inches and concentrated torques at two wing span stations $y = 60.75$ inches and $y = 35.25$ inches. The deflections and twist about the wing pitch axis y at the six measurement stations were measured by the VICON systems. Figures 24 to 27 are the plots of the deflections and twists measured from the static load tests. The twist measurements at station $y = 35.25$ inches were not shown since the data were taken with only one torque input of 95 in-lb and exhibit a considerable scatter. Figure 27 shows that the static load test in torsion is not in pure torsion as the measured deflections under the applied torque are not zero.

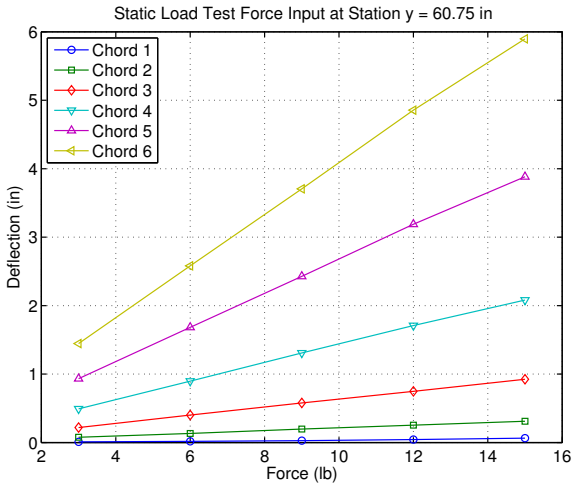

Fig. 24 - Static Deflection Measurements for Force Input @ $y = 60.75$ inches

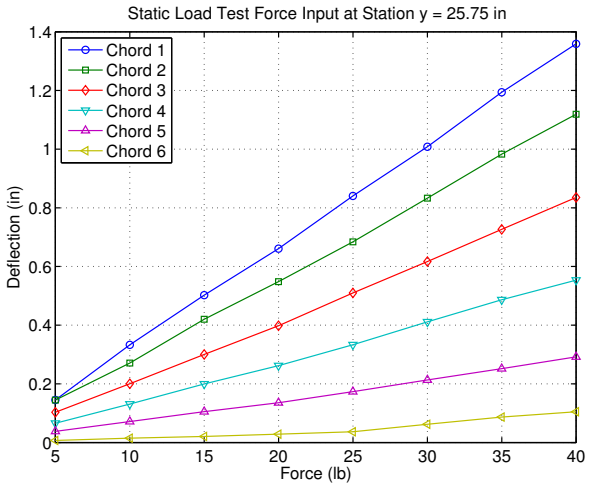

Fig. 25 - Static Deflection Measurements for Force Input @ $y = 25.75$ inches

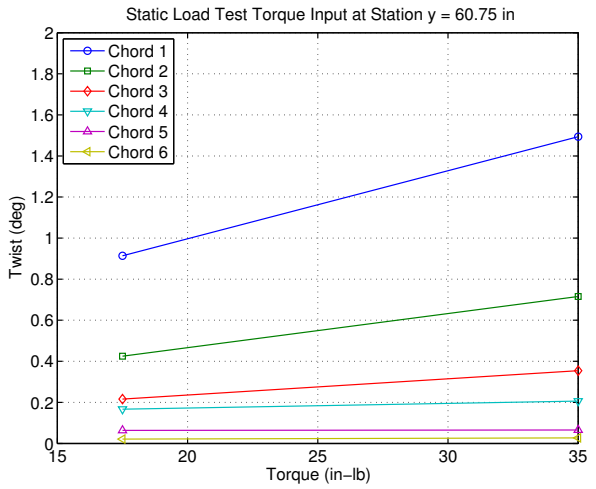

Fig. 26 - Static Twist Measurements for Torque Input @ $y = 60.75$ inches

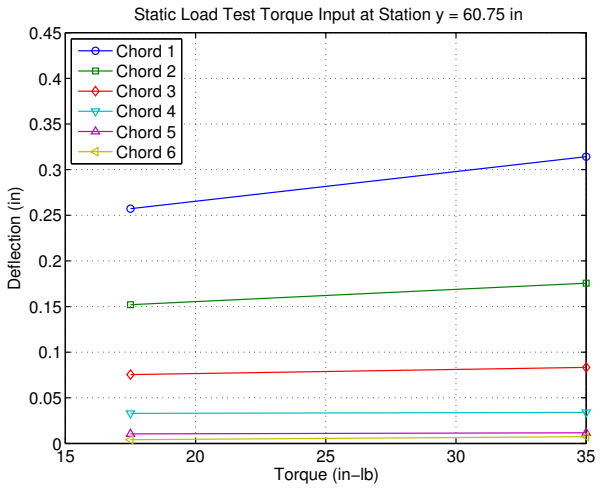

Fig. 27 - Static Deflection Measurements for Torque Input @ $y = 60.75$ inches

The data from the static load and modal analysis tests were used to validate a 3D NASTRAN static and modal analysis models built by UWAL.[6] A stick NASTRAN static model was then constructed by UWAL to provide the equivalent bending and torsion stiffnesses of the wing. The stick NASTRAN model represents the wing as a series of beam sections at varying sweep angles to account for changes in the wing stiffness across the wing span, as shown in Fig. 28. Figures 29 and 30 are the plots of the bending and torsion stiffnesses for the UWAL stick NASTRAN model. The wing is significant stiffer in torsion than in bending as can be seen from Figs. 29 and 30. The torsional stiffness at the wing tip is observed to be very large. This could be due to structural reinforcements and flap support structures at the wing tip.

Both the 3D NASTRAN and stick NASTRAN models were provided to NASA Ames Research Center by UWAL. In addition, UWAL also provided the static deflections computed by the 3D NASTRAN model. NASA Ames Research Center later ran the UWAL stick NASTRAN model to obtain the static deflections. Both the static deflections computed by the stick NASTRAN model and 3D NASTRAN were then compared against the static deflection measurements, as shown in Figs. 31 and 32. The static deflections computed by the 3D NASTRAN are in very good agreement with the static deflection measurements. However, the static deflections computed by the stick NASTRAN model have poor agreement with the static deflection measurements for the applied force at station $y = 25.75$ inches. The agreement for the applied force at the other station is reasonably good. This is a result of the UWAL stick model generated, as a preliminary model, with more weight in the stiffness fitting placed on outboard wing behavior of static aeroelastic and dynamic modal importance, including capturing local "jumps" in stiffness in areas of backbone structure, stiff edges, and hard attachment points, as well as geometrical breaks in the wing (see Figure 8).

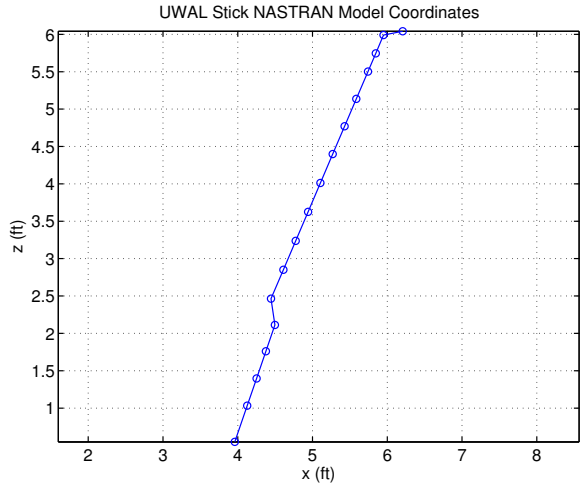

Fig. 28 - Nodal Coordinates of UWAL Stick NASTRAN Model ($z = 0$ from Tunnel Floor)

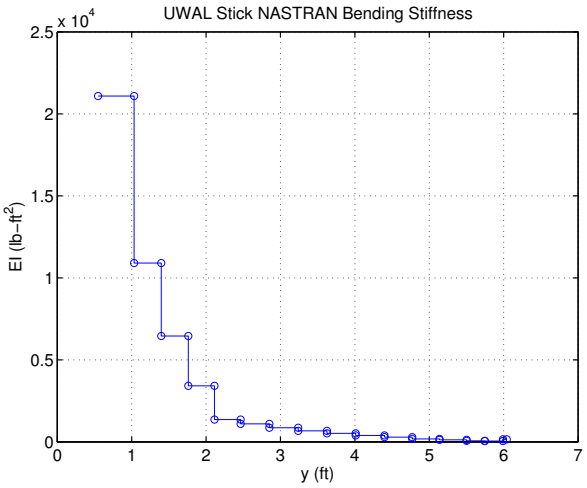

Fig. 29 - UWAL Stick NASTRAN Bending Stiffness

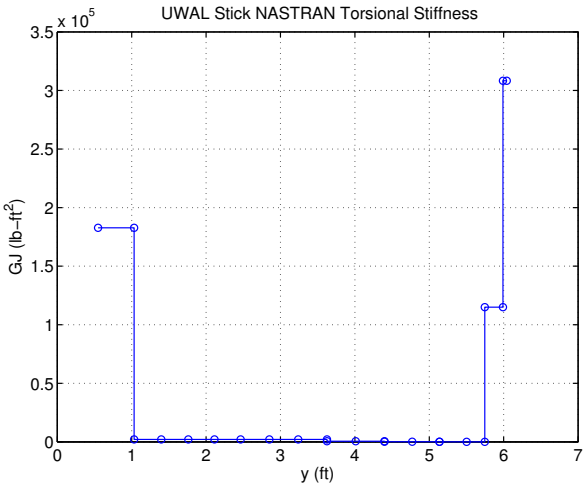

Fig. 30 - UWAL Stick Model Torsional Stiffness

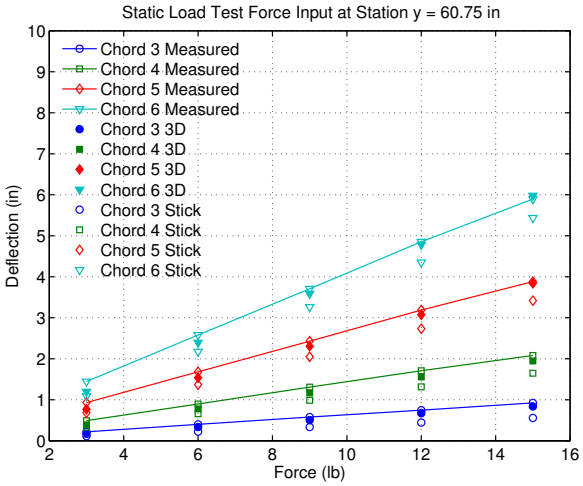

Fig. 31 - NASTRAN Static Deflections for Force Input @ $y = 60.75$ inches

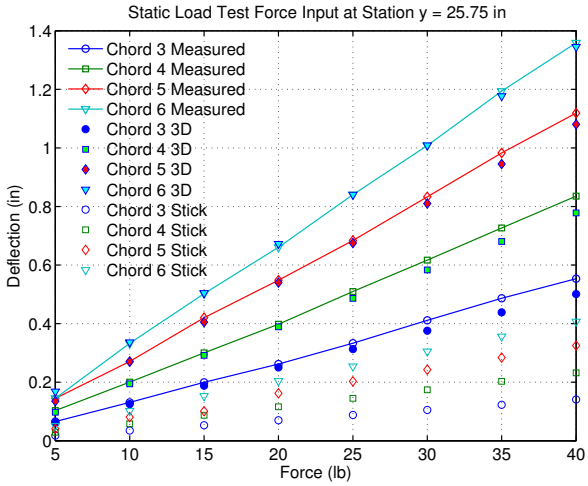

Fig. 32 - NASTRAN Static Deflections for Force Input @ $y = 25.75$ inches

In order to work with a stick model that would capture static behavior well along inboard as well as outboard sections of the wing and that would not have the stiffness discontinuities of Fig. 30, a smooth continuous stiffness stick model was sought. The procedure used was based on an optimization problem solution that would minimize displacement errors for the loaded wing between the new stick model and the detailed 3D NASTRAN model.

The static deflection is computed using the Galerkin's method by assuming the following solution:

$$\Theta(\bar{y}) = \Psi(\bar{y})\,\theta \tag{40}$$

$$W(\bar{y}) = \Phi(\bar{y})\,w \tag{41}$$

where $\theta = \begin{bmatrix} \theta_1 & \dots & \theta_n \end{bmatrix}^\top$ and $w = \begin{bmatrix} w_1 & \dots & w_n \end{bmatrix}^\top$ are vectors of generalized coordinates, and $\Psi(\bar{y}) = \begin{bmatrix} \psi_1(\bar{y}) & \dots & \psi_n(\bar{y}) \end{bmatrix}$ and $\Phi(\bar{y}) = \begin{bmatrix} \phi_1(\bar{y}) & \dots & \phi_n(\bar{y}) \end{bmatrix}$ are shape functions selected to be the natural mode shapes of a uniform cantilever beam which are given by

$$\psi_i(\bar{y}) = \sqrt{2}\sin\frac{(2i-1)\,\pi\bar{y}}{2L} \tag{42}$$

$$\phi_i(\bar{y}) = \cosh(\beta_i\bar{y}) - \cos(\beta_i\bar{y}) - \frac{\cosh(\beta_i L) + \cos(\beta_i L)}{\sinh(\beta_i L) + \sin(\beta_i L)}\left[\sinh(\beta_i\bar{y}) - \sin(\beta_i\bar{y})\right] \tag{43}$$

where $\beta_i L$ are the eigenvalues corresponding to their natural mode shapes of beam bending.

Then the bending and torsional deflections are computed as

$$\theta = K_\theta^{-1} F_\theta \tag{44}$$

$$w = K_w^{-1} F_w \tag{45}$$

where K_θ and K_w are the torsional and bending generalized stiffnesses, respectively, and F_θ and F_w are the torsional and bending generalized forces, respectively, which are defined as

$$K_\theta = \int_0^L GJ \frac{d\Psi^\top(\bar{y})}{d\bar{y}} \frac{d\Psi(\bar{y})}{d\bar{y}} d\bar{y} \tag{46}$$

$$K_w = \int_0^L EI \frac{d^2\Phi^\top(\bar{y})}{d\bar{y}^2} \frac{d^2\Phi(\bar{y})}{d\bar{y}^2} d\bar{y} \tag{47}$$

$$F_\theta = \Psi^\top(\bar{y}_M) M \tag{48}$$

$$F_w = \Phi^\top(\bar{y}_P) P \tag{49}$$

where M and P are the concentrated applied torque at $\bar{y} = \bar{y}_M$ and applied force at $\bar{y} = \bar{y}_P$.

For the estimation of the wing stiffness, the static deflections are all normalized to a unit value at the Chord 6 station. Thus, the applied forces and applied torque are computed to correspond to these normalized static deflections. Furthermore, the torsional deflections about the elastic axis $\bar{y}$ are computed from the twist measurements are with respect to the wing pitch axis y and the bending deflection measurements according to

$$\Theta_i = \frac{\varphi_i}{\cos\Lambda} - W_i \tan\Lambda \tag{50}$$

where φ_i is the measured twist about the wing pitch axis y at the Chord i station.

A linear regression is performed to compute the normalized static deflections and applied forces and torque as follows:

$$\bar{\Theta}_i = \left(\frac{\Delta\Theta}{\Delta M}\right)_i \bar{M} + \Delta\Theta_i \tag{51}$$

$$\bar{W}_i = \left(\frac{\Delta W}{\Delta P}\right)_i \bar{P} + \Delta W_i \tag{52}$$

$$\bar{M} = \frac{1 - \Delta\Theta_6}{\left(\frac{\Delta\Theta}{\Delta M}\right)_i} \tag{53}$$

$$\bar{P} = \frac{1 - \Delta W_6}{\left(\frac{\Delta W}{\Delta P}\right)_6} \tag{54}$$

where $\left(\frac{\Delta\Theta}{\Delta M}\right)_i$, $\left(\frac{\Delta W}{\Delta P}\right)_i$, ΔW_i and $\Delta\Theta_i$ are obtained from the linear regression of the static deflection measurements as functions of the applied forces and torque.

The optimization is set up to minimize two cost functions to estimate the bending and torsional stiffnesses as follows:

$$J_W = \sum_{i=1}^{6} \left(\hat{W}_i - \bar{W}_i\right)^2 \Bigg|_{\bar{P}@y=60.75} + \sum_{i=1}^{6} \left(\hat{W}_i - \bar{W}_i\right)^2 \Bigg|_{\bar{P}@y=25.75} \tag{55}$$

$$J_\Theta = \sum_{i=1}^{6} \left(\hat{\Theta}_i - \bar{\Theta}_i\right)^2 \Bigg|_{\bar{M}@y=60.75} \tag{56}$$

A cubic polynomial shape function is chosen to be a design shape function. This shape function is applied as a multiplier to the baseline UWAL bending stiffness in the stick NASTRAN model. Thus, the design variables are the four polynomial coefficients of the shape function. A gradient search is conducted to identify the optimal shape functions that minimize the cost functions for the bending and torsional deflections. Because of the strange behavior in the UWAL torsional stiffness as represented in the stick NASTRAN model, the optimization does not converge properly. As a result, it is decided that the baseline torsional stiffness in the optimization assumes the same spatial distribution as the bending stiffness. The optimization then converges to the bending and torsional stiffnesses, as shown in Figs. 33 and 34. The ratio of the torsional stiffness to the bending stiffness is about 3:1, which indicates that the UWAL wind tunnel model is significantly stiffer in torsion than in bending. This is consistent with the aeroelastic deflection measurements. The optimization also shows that the optimization results depend on the initialization. Consequently, variations in the estimated stiffness are expected.

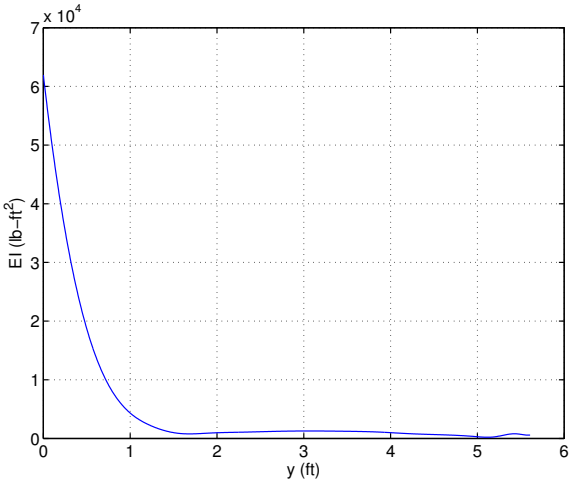

Fig. 33 - Optimized Bending Stiffness of UWAL Flexible Wing Wind Tunnel Model

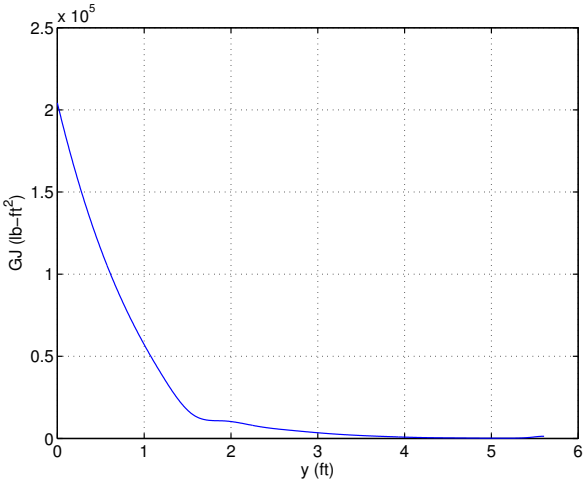

Fig. 34 - Optimized Torsional Stiffness of UWAL Flexible Wing Wind Tunnel Model

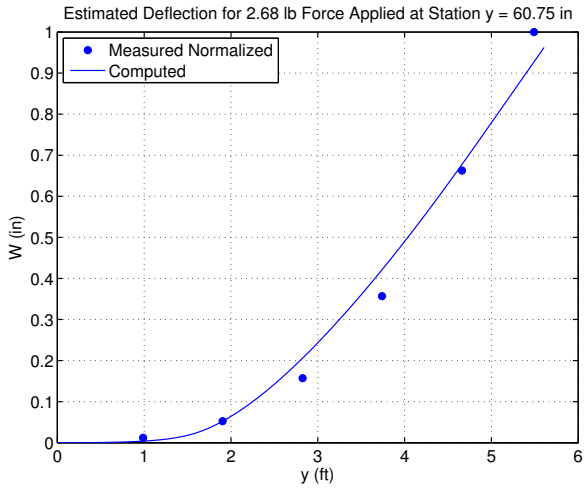

Fig. 35 - Computed vs. Measured Normalized Static Deflections for Force Input @ $y = 60.75$ inches

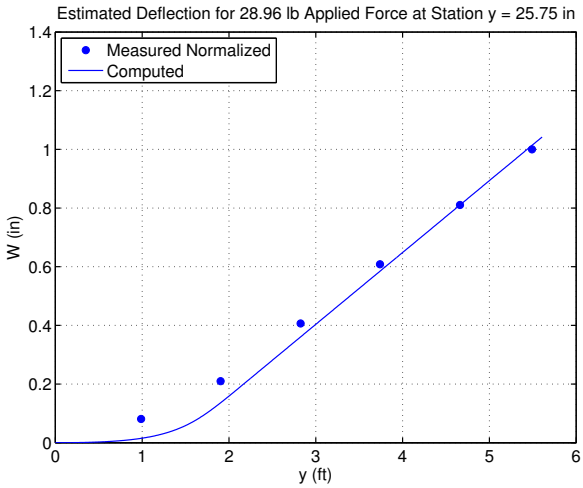

Fig. 36 - Computed vs. Measured Normalized Static Deflections for Force Input @ $y = 25.75$ inches

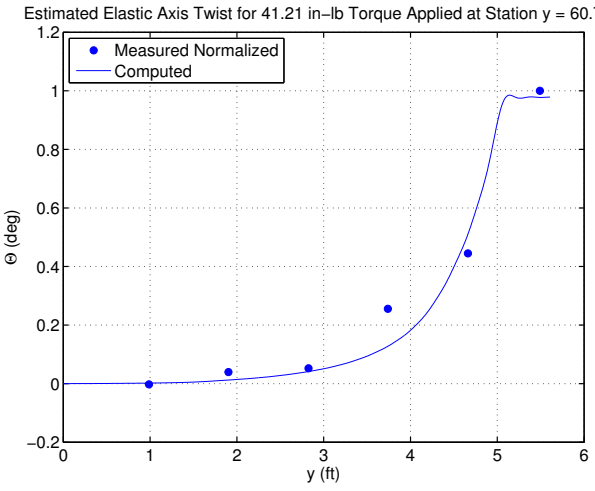

Fig. 37 - Computed vs. Measured Normalized Static Torsional Deflections for Torque Input @ $y = 60.75$ inches

Figures 35 to 37 present the comparisons between the computed static deflections against the normalized static deflections computed directly from the measured static deflections. The agreements between the computed and the measured normalized static deflections are excellent

Using the optimized stiffnesses, a coupled aerodynamic-structural modeling approach is conducted using the finite-element method coupled with the vortex-lattice method to predict the aerodynamic performance of the UWAL flexible wing wind tunnel model.

VII. Coupled Aerodynamic-Structural Modeling

To establish the aerodynamic analysis, a vortex-lattice aerodynamic solver, Vorlax, is used to compute the aerodynamic characteristics of the UWAL flexible wing wind tunnel model. Vorlax is an aerodynamic performance prediction code, developed by Miranda et al,[17] that provides a rapid method for estimating force and moment coefficients as well as stability and control derivatives of an aerodynamic configuration. An aerodynamic configuration is constructed within Vorlax by a series of lifting panels that are formed by spanwise and chordwise locations of vortices based on the locations of the computing stations specified by the user. Vorlax computes the vehicle aerodynamics in both the longitudinal and lateral directions independently. The longitudinal and lateral computational results are then combined to produce overall aerodynamic characteristics of an aerodynamic configuration at any arbitrary angles of attack and sideslip. It is based on the vortex-lattice method. Vorview is a graphical user interface front end that allows users to create a model and execute Vorlax interactively or in a batch mode.

Because the vortex-lattice method is based on potential flow theory, it is an inviscid code that can only compute inviscid drag due to lift. It cannot predict viscous or wave drag. The compressibility effect on the aerodynamic coefficients is corrected by the Prandtl-Glauert compressibility correction. For lift prediction at low angle of attack, Vorlax can provide reasonably accurate prediction. Figure 38 shows a comparison between the lift coefficient predicted by Vorlax and the measured lift coefficient of a sub-scale 5.5% wind tunnel model of the GTM tested in NASA Langley Research Center's 14-Foot-By-22-Foot Wind Tunnel.[15] The agreement between the Vorlax lift prediction and test data is excellent.

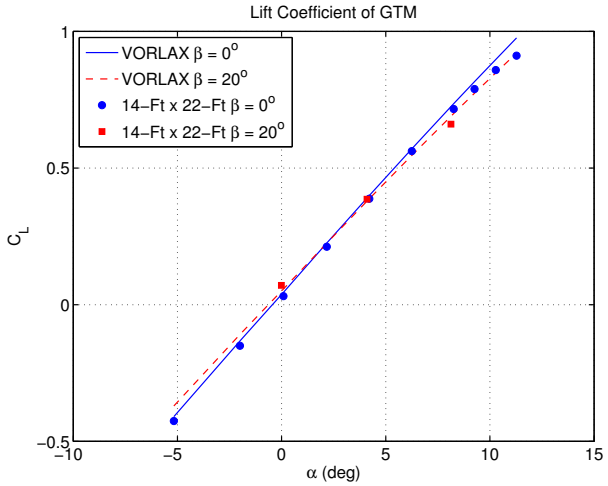

Fig. 38 - Lift Curve for NASA GTM

The UWAL flexible wing wind tunnel constructed in Vorlax is shown in Fig. 39. The model has the wing and fuselage components. The wing component is defined by a series of wing sections in the directions parallel to the aircraft axis and parallel to the edges of the VCCTEF. The fuselage component is defined by a series of closed sections in the $y-z$ plane of the aircraft. A geometry tool, written in MATLAB, provides the ability to model the VCCTEF by deforming the trailing edge portion of the wing panels on which the VCCTEF is defined. The geometry tool creates the rotation of each of the three camber segments by a specified flap deflection. The trailing edge portion of the wing section that includes the VCCTEF thus is modified by the rotation of the three camber segments. Furthermore, the geometry tool also provides the ability to deform the wing geometry on the flight in all three directions: flapwise bending, chordwise bending, and twist. The deformation capability of the geometry tool allows a finite-element model to couple directly to Vorview for coupled aerodynamic-structural modeling.[16]

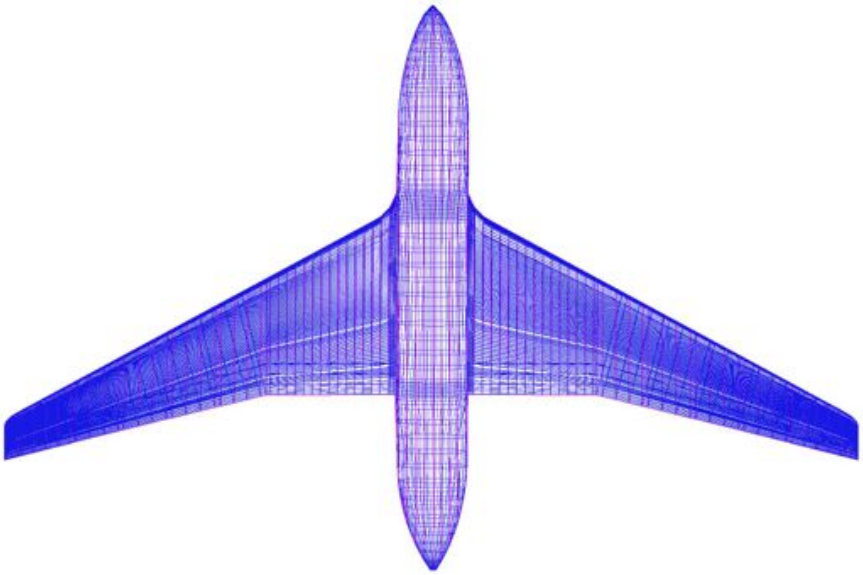

Fig. 39 - UWAL Wind Tunnel Model in Vorview

The UWAL model is set up with the panels sub-divided into 2000 sub-polygons. The flat plate option is set to off to properly model the camber lifting surfaces of the model. Vorlax execution in the batch mode is controlled via a MATLAB script that handles the interfaces with the geometry tool and a finite-element code, also written in MATLAB. The finite-element code is fully capable of performing static and dynamic aeroelasticity using three dimensional beam elements to model wing structures. The detail development of the aeroelastic finite-element modeling is described in a paper by Nguyen, Ting, et al.

Vorlax computes aerodynamic forces and moments which are then transferred to the finite-element model (FEM). The finite-element code then computes the wing aeroelastic deflections which are then passed to the geometry tool. The Vorlax geometry file .hrm is then directly modified by the geometry tool which changes the geometry to model the aeroelastic deflections. The new geometry file is then read by Vorview which calls Vorlax to execute the computation. This iterative process continues until a convergence criterion is met.

The lift and drag characteristics of the rigid wing reference geometry from which the wind tunnel model is constructed are first computed by Vorlax without structural coupling. Figure 40 is the lift curve of the rigid baseline FLAP0 configuration. For comparison, the rigid wing lift curves of the baseline FLAP0 configuration computed by Euler CFD code Cart3D[10] and estimated from the UWAL wind tunnel test data by the dynamic pressure and the aeroelastic deflection correction methods[13] are also plotted. It can be seen that Vorlax under-predicts lift for the rigid wing UWAL wind tunnel model by some amount. The lift prediction of FLAP0 configuration by Vorlax is still reasonably in good agreement with the dynamic pressure corrected wind tunnel test data.

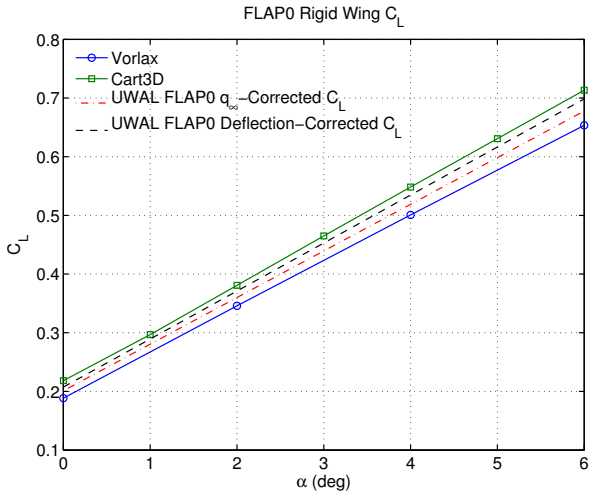

Fig. 40 - Rigid Wing FLAP0 Lift Curves

The VCCTEF segment angles during the test were set using stiff aluminum tape and measured carefully before and after each wind-on run to identify any drift or deviation from the desired angles. Aluminum tape hinge stiffness was measured, and, given the low loads on the VCCTEF segments, it was expected that static aeroelastic deviation from the pre-set angles during wind-on conditions would be negligible. While there were VICON reflective dots on all VCCTEF segments, the size of the dots and the small distances chordwise between the dots made VICON measurements of the VCCTEF segment angles unreliable. In follow-up tests of a high-lift VCCTEF wing configuration, the VCCTEF angle setting design was modified to remove any uncertainty in the VCCTEF segment angles.[17] Nevertheless, studies were carried out to assess the influence of some uncertainty in the VCCTEF segment angle settings on the test results for the cruise configuration.[6] For the present study, uncertainty based on the VCCTEF measured angles was nevertheless used as an upper bound on the uncertainties expected. Table 5 summarizes the VCCTEF deflection measurements for the baseline FLAP0 configuration. These measurements indicate variations in the VCCTEF deflection with a mean of about 1 degree.

Run	1A	1B	1C	2A	2B	2C	3A	3B	3C	4A	4B	4C	5A	5B	5C
18	-0.1	0.0	-0.3	0.4	-1.1	2.1	-0.2	-1.1	2.6	-1.9	2.9	-2.1	0.6	-0.9	1.5
19	0.3	0.0	0.2	0.0	0.4	0.8	1.0	-2.4	4.7	-0.1	1.2	-1.2	-0.3	1.4	-0.1
20	0.7	0.1	0.3	0.4	-0.2	1.7	0.5	-0.9	3.4	0.4	1.1	-0.7	0.2	1.1	-0.8
21	0.0	0.1	0.2	-0.1	0.2	0.1	-0.2	-0.7	3.4	-0.7	0.9	-0.5	0.6	0.4	1.2
22	0.5	-0.3	0.4	0.4	-0.6	0.7	-0.5	-0.1	2.2	-0.8	0.6	-0.1	1.6	-1.5	3.7
23	1.7	0.5	1.1	1.6	0.4	2.3	1.6	-1.0	5.4	2.4	0.2	2.2	2.7	-1.6	3.8
24	1.9	0.6	1.2	1.9	0.1	3.3	2.5	-1.2	5.0	2.1	1.8	0.1	1.7	-0.7	4.1
69	0.3	0.2	-0.5	0.7	-0.7	0.8	0.4	-0.4	1.1	-0.6	1.1	-0.9	1.3	-0.8	-1.5
70	1.0	0.0	0.9	0.7	0.8	0.4	1.0	-1.2	3.9	0.0	1.8	-0.9	1.7	-2.1	1.7
71	1.5	0.5	0.7	1.7	0.3	1.7	1.2	0.6	1.5	1.4	0.6	1.4	1.5	0.3	-0.3
72	2.2	0.9	0.6	3.0	0.0	2.6	1.8	1.7	0.4	2.8	1.4	0.5	2.1	-0.8	1.8
Mean	0.91	0.24	0.44	0.97	-0.04	1.50	0.83	-0.61	3.05	0.45	1.24	-0.20	1.25	-0.47	1.37

Table 5 - VCCTEF Deflection Measured by VICON System for FLAP0 Configuration

The lift prediction taking into account of the uncertainty in the indicated VCCTEF deflections is shown in Fig. 41. It is interesting to note that the variations in the indicated VCCTEF deflection are uni-directional in that they result in a higher lift prediction than the baseline lift coefficient for the reference FLAP0 VCCTEF deflection. The estimated rigid wing lift curves fall within the uncertainty band of the lift prediction. It is observed that the lift prediction for the mean indicated VCCTEF deflection agrees very well with the rigid wing lift estimated by the aeroelastic deflection correction method. The spread in the lift prediction based on the indicated VCCTEF deflections is rather large. The experimental lift data, however, shows a high degree of correlation. This suggests that the actual variations in the VCCTEF deflection may be smaller than as indicated by the VICON measurements. Without the knowledge of the true VCCTEF deflections, it may be difficult to assess the accuracy of the tool for lift prediction. Given that any uncertainty in the VCCTEF deflection will result in a constant offset in the lift coefficient, therefore this suggests that the lift curve slope may be a better indication for comparing the lift prediction. The predicted rigid wing lift curve slope is calculated to be $C^*_{L_\alpha} = 4.4401$ for the baseline FLAP0 configuration which agrees well with the estimated rigid wing lift curve slopes of $C^*_{L_\alpha} = 4.5533$ and $C^*_{L_\alpha} = 4.7488$ by the dynamic pressure and aeroelastic deflection correction methods, respectively. The difference ranges from 2.5% to 6.5%.

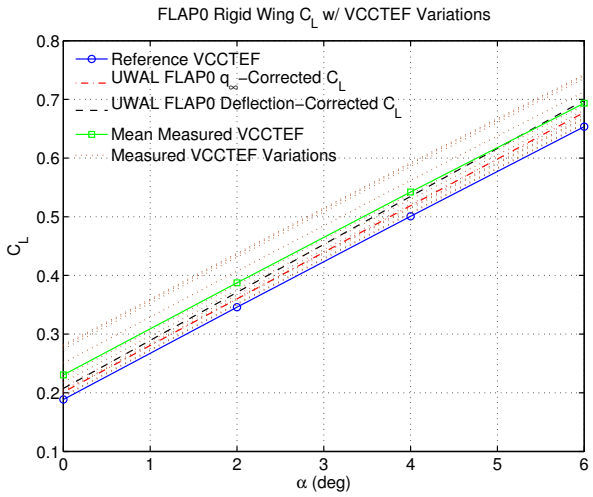

Fig. 41 - Rigid Wing FLAP0 Lift Curves for Variations in VCCTEF Deflection

The lift prediction of the flexible wing UWAL wind tunnel model is computed next using the coupled Vorlax-FEM. Figure 42 shows the lift prediction of the flexible wing UWAL wind tunnel model by Vorlax for the reference FLAP0 VCCTEF and the mean VCCTEF deflections. The lift curve for the mean VCCTEF deflection agrees very well with the measured lift curve in the wind tunnel. The predicted lift curve slopes of $C_{L_\alpha} = 4.0229$ and $C_{L_\alpha} = 4.0267$ for the reference FLAP0 VCCTEF and the mean VCCTEF deflections, respectively, are in excellent agreement with the measured lift curve slope of $C_{L_\alpha} = 4.1482$ with errors of about 3%.

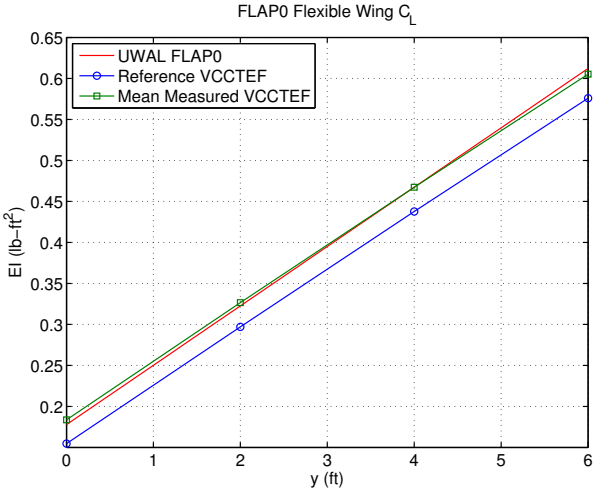

Fig. 42 - Flexible Wing FLAP0 Lift Curves

Figures 43 shows the bending deflections computed for the reference geometry of FLAP0 configuration with and without the mean VCCTEF deflection as compared to the measured bending deflection in the UWAL for an angle of attack of 6°. The computed bending deflections in general agree well with the measured bending deflection. The bending deflection at the wing tip for the baseline FLAP0 configuration matches the measured value. The wing tip bending deflection at an angle of attack of 6° is about 11% of the wing semi-span. This is similar to the flexibility of modern transport wings. Figure 44 is the plot of the wash-out twist about the wing pitch axis due to the wash-out effect of wing bending and the torsional deflection about the elastic axis. The aeroelastic deflection measurements in UWAL indicate that the wash-out twist is primarily due to the bending deflection, while torsional deflection contributes very little to the wash-out twist because the wing is significantly stiffer in torsion than in bending. The computed wash-out twist for the baseline FLAP0 configuration shows a good agreement with the measured wash-out twist at the wing tip, but exhibits a greater discrepancy along the wing span by as much as 0.7°. It should be noted that the wash-out twist measurements by the VICON are considered to be less accurate than the wing bending deflection measurements.

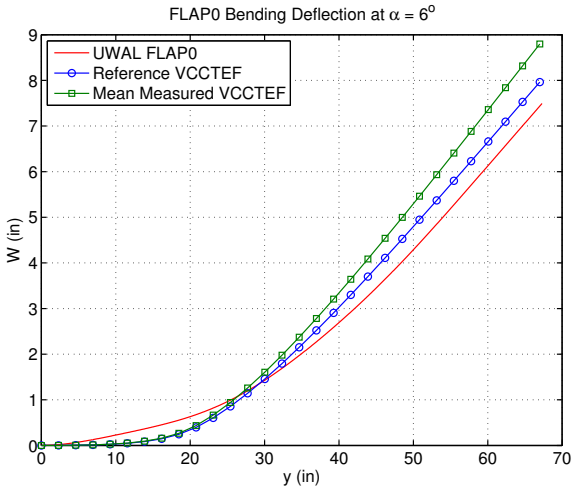

Fig. 43 - Flexible Wing FLAP0 Bending Deflection for $\alpha = 6^o$

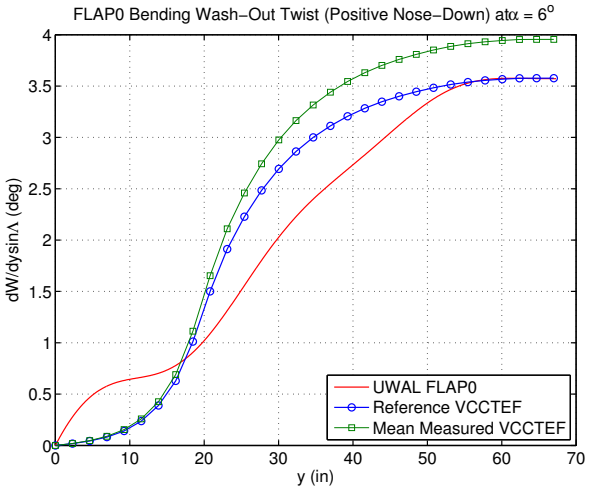

Fig. 44 - Flexible Wing FLAP0 Bending Wash-Out Twist (Positive Nose-Down) about Wing Pitch Axis for $\alpha = 6^o$

VIII. Conclusion

This paper presents an aeroelastic analysis of a flexible wing wind tunnel model with a variable camber continuous trailing edge flap (VCCTEF) design for drag minimization tested at the University of Washington Aeronautical Laboratory (UWAL). The wind tunnel test was designed to explore the relative merit of the VCCTEF concept for improved cruise efficiency. The VCCTEF is a multi-segment flap design having three chordwise camber segments and five spanwise flap sections for a total of 15 flap segments. Elastomeric material is used to cover the gaps in between the spanwise flap sections, thereby creating a continuous trailing edge. The flexible wing model is a 10%-scale model of a typical transport wing. The wing structural stiffness in bending is tailored to achieve a wing tip deflection of about 10% of the wing semi-span. A method for estimating the bending and torsional stiffnesses of the flexible wing UWAL wind tunnel model from static load test data has been developed. The resulting estimation indicates that the stiffness of the flexible wing is significantly stiffer in torsion than in bending by as much as 3 to 1. Variations in the estimated stiffness can result depending on the initialization of the optimization. This can result in uncertainty which is not included in the analysis. The lift prediction for the flexible wing is computed by a coupled aerodynamic-structural model. The coupled model is developed by coupling a conceptual aerodynamic tool Vorlax with a finite-element model of the flexible wing via an automated geometry deformation tool. Based on the comparison of the lift curve slope, the lift prediction for the rigid wing is in good agreement with the estimated lift coefficients derived from the wind tunnel test data. Due to the movement of the VCCTEF during the wind tunnel test, uncertainty in the lift prediction due to the indicated variations of the VCCTEF deflection is studied. The results show a significant spread in the lift prediction which contradicts the consistency in the aerodynamic measurements, thus suggesting that the indicated variations as measured by the VICON system may not be reliable. The lift prediction of the flexible wing agrees well with the measured lift curve for the baseline configuration. The computed bending deflection and wash-out twist of the flexible wing also match reasonably well with the aeroelastic deflection measurements. The results demonstrate the validity of the aerodynamic-structural tool for use to analyze aerodynamic performance of flexible wings.

Acknowledgment

The authors would like to thank the Fixed Wing / Advanced Air Transport Technology Project under the Fundamental Aeronautics Program of NASA Aeronautics Research Mission Directorate (ARMD) for funding support of this work. The authors also would like to acknowledge Boeing Research and Technology and University of Washington for their collaboration with NASA under NASA contract NNL12AD09T entitled "Development of Variable Camber Continuous Trailing Edge Flap System for B757 Configured with a More Flexible Wing."

References

[1]Nguyen, N., "Elastically Shaped Future Air Vehicle Concept," NASA Innovation Fund Award 2010 Report, October 2010, Submitted to NASA Innovative Partnerships Program.

[2]Nguyen, N., Trinh, K., Reynolds, K., Kless, J., Aftosmis, M., Urnes, J., and Ippolito, C., "Elastically Shaped Wing Optimization and Aircraft Concept

for Improved Cruise Efficiency," AIAA Aerospace Sciences Meeting, AIAA-2013-0141, Grapevine, TX, January 2013.

[3]Boeing Report No. 2012X0015, "Development of Variable Camber Continuous Trailing Edge Flap System," October 4, 2012.

[4]Urnes, J., Nguyen, N., Ippolito, C., Totah, J., Trinh, K., and Ting, E., "A Mission Adaptive Variable Camber Flap Control System to Optimize High Lift and Cruise Lift to Drag Ratios of Future N+3 Transport Aircraft," AIAA Aerospace Sciences Meeting, AIAA-2013-0214, Grapevine, TX, January 2013.

[5]Jordan, T. L., Langford, W. M., Belcastro, C. M., Foster, J. M., Shah, G. H., Howland, G., and Kidd, R., "Development of a Dynamically Scaled Generic Transport Model Testbed for Flight Research Experiments," AUVSI Unmanned Unlimited, Arlington, VA, 2004.

[6]Precup, N., Mor, M., and Livne, E., "Design, Construction, and Tests of an Aeroelastic Wind Tunnel Model of a Variable Camber Continuous Trailing Edge Flap (VCCTEF) Concept Wing," 32nd AIAA Applied Aerodynamics Conference, 2014-2442, Atlanta, GA, June 2014, doi: 10.2514/6.2014-2442.

[7]Bisplinghoff, R. L, Ashley, H., and Halfman, R. L, *Aeroelasticity*, Addison-Wesley, 1955, pp. 478 - 480.

[8]Anderson, J. D., *Fundamentals of Aerodynamics*, McGraw-Hill, 2001, pp. 289 - 310.

[9]Hodges, D. and Pierce, G., *Introduction to Structural Dynamics and Aeroelasticity*, Cambridge University Press, 2002.

[10]Rodriguez, D., Aftosmis, M., Nemec, M., and Smith, S., "Static Aeroelastic Analysis with an Inviscid Cartesian Method," AIAA Science and Technology Forum, AIAA-2014-0836, National Harbor, MD, January 2014.

[11]Nguyen, N., Ting, E., Nguyen, D., Dao, T., and Trinh, K., "Coupled Vortex-Lattice Flight Dynamic Model with Aeroelastic Finite-Element Model of Flexible Wing Transport Aircraft with Variable Camber Continuous Trailing Edge Flap for Drag Reduction," AIAA Atmospheric Flight Mechanics, AIAA-2013-4746, Boston, MA, August 2013.

[12]Ting, E., Nguyen, N., and Trinh, K., "Static Aeroelastic and Longitudinal Trim Model of Flexible Wing Aircraft Using Finite-Element Vortex-Lattice Coupled Solution," 55th AIAA/ASME/ASCE/AHS/ASC Structures, Structural Dynamics, and Materials Conference, AIAA-2014-0837, National Harbor, MD, January 2014.

[13]Nguyen, N., Precup, N., Urnes, J., Nelson, C., Lebofsky, S., Ting, E., and Livne, E., "Experimental Investigation of a Flexible Wing with a Variable Camber Continuous Trailing Edge Flap Design," 32nd AIAA Applied Aerodynamics Conference, AIAA 2014-2441, Atlanta, GA, June 2014.

[14]Miranda, L.R., Elliot, R.D., and Baker, W.M., "A Generalized Vortex Lattice Method for Subsonic and Supersonic Flow Applications," NASA CR-2865, 1977.

[15]Nguyen, N. T., Nelson, A., and Pulliam, T., "Damage Adaptive Control System Research Report," Internal NASA Report, April 2006.

[16]Ting, E., Nguyen, N., and Lebofsky, S., "Static Aeroelastic Modeling of a Sub-Scale Wind Tunnel Model with Novel Flap Concept," 56th AIAA/ASME/ASCE/AHS/ASC Structures, Structural Dynamics, and Materials Conference, AIAA-2015-1407, Kissimmee, FL, January 2015.

[17]Precup, N., Mor, M., and Livne, E., "The Design, Construction, and Tests of a Concept Aeroelastic Wind Tunnel Model of a High-Lift Variable Camber Continuous Trailing Edge Flap (HL-VCCTEF) Wing Configuration", 56th AIAA/ASME/ASCE/AHS/ASC Structures, Structural Dynamics, and Materials Conference, AIAA 2015-1406, Kissimmee, FL, January 2015, doi: 10.2514/6.2015-1406.